HHS Public Access

Author manuscript

Cell Rep. Author manuscript; available in PMC 2022 January 01.

Published in final edited form as:

Cell Rep. 2021 December 14; 37(11): 110110. doi:10.1016/j.celrep.2021.110110.

YTHDC2 is essential for pachytene progression and prevents aberrant microtubule-driven telomere clustering in male meiosis

Rong Liu[1,2], **Seth D. Kasowitz**[2], **David Homolka**[3], **N. Adrian Leu**[2], **Jordan T. Shaked**[2], **Gordon Ruthel**[4], **Devanshi Jain**[5,6], **Huijuan Lin**[1,2], **Scott Keeney**[5,7], **Mengcheng Luo**[1], **Ramesh S. Pillai**[3], **P. Jeremy Wang**[2,8,*]

[1]School of Basic Medical Sciences, Wuhan University, Wuhan, Hubei Province, China

[2]Department of Biomedical Sciences, University of Pennsylvania School of Veterinary Medicine, Philadelphia, PA, USA

[3]Department of Molecular Biology, Science III, University of Geneva, CH-1211 Geneva 4, Switzerland

[4]Department of Pathobiology, University of Pennsylvania School of Veterinary Medicine, Philadelphia, PA, USA

[5]Molecular Biology Program, Memorial Sloan Kettering Cancer Center, New York City, NY, USA

[6]Department of Genetics, Rutgers University, Piscataway, NJ, USA

[7]Howard Hughes Medical Institute, Memorial Sloan Kettering Cancer Center, New York City, NY, USA

[8]Lead contact

SUMMARY

Mechanisms driving the prolonged meiotic prophase I in mammals are poorly understood. RNA helicase YTHDC2 is critical for mitosis to meiosis transition. However, YTHDC2 is highly expressed in pachytene cells. Here we identify an essential role for YTHDC2 in meiotic progression. Specifically, YTHDC2 deficiency causes microtubule-dependent telomere clustering and apoptosis at the pachytene stage of prophase I. Depletion of YTHDC2 results in a massively dysregulated transcriptome in pachytene cells, with a tendency toward upregulation of genes normally expressed in mitotic germ cells and downregulation of meiotic transcripts. Dysregulation does not correlate with m^{6}A status, and YTHDC2-bound mRNAs are enriched

*Correspondence: pwang@upenn.edu.

AUTHOR CONTRIBUTIONS

P.J.W., R.L., and S.D.K. conceptualized the study and designed the experiments. R.L. performed most of the experiments. M.L. identified YTHDC2. S.D.K. generated the *Ythdc2 floxed* mice. N.A.L. performed blastocyst injection of targeted ES cells. S.D.K. and J.S. generated the *Ythdc2*$^{fl/-}$ *Ddx4-Cre*^{ERT2} mice. D.H. and R.S.P. analyzed the RNA-seq data. G.R. contributed to microscopy and performed 3D deconvolution. D.J. and S.K. generated the *Ythdc2*$^{fl/em1}$ *Ngn3*-Cre data. P.J.W. and R.L. wrote the manuscript.

DECLARATION OF INTERESTS

The authors declare no competing interests.

SUPPLEMENTAL INFORMATION

Supplemental information can be found online at https://doi.org/10.1016/j.celrep.2021.110110.

in genes upregulated in mutant germ cells, revealing that YTHDC2 primarily targets mRNAs for degradation. Furthermore, altered transcripts in mutant pachytene cells encode microtubule network proteins. Our results demonstrate that YTHDC2 regulates the pachytene stage by perpetuating a meiotic transcriptome and preventing microtubule network changes that could lead to telomere clustering.

In brief

Mechanisms driving the prolonged meiotic prophase I in mammals are poorly understood. Liu et al. show that RNA helicase YTHDC2 regulates the pachytene stage of meiotic prophase I by perpetuating a meiotic transcriptome and preventing microtubule network changes that could lead to telomere clustering.

Graphical Abstract

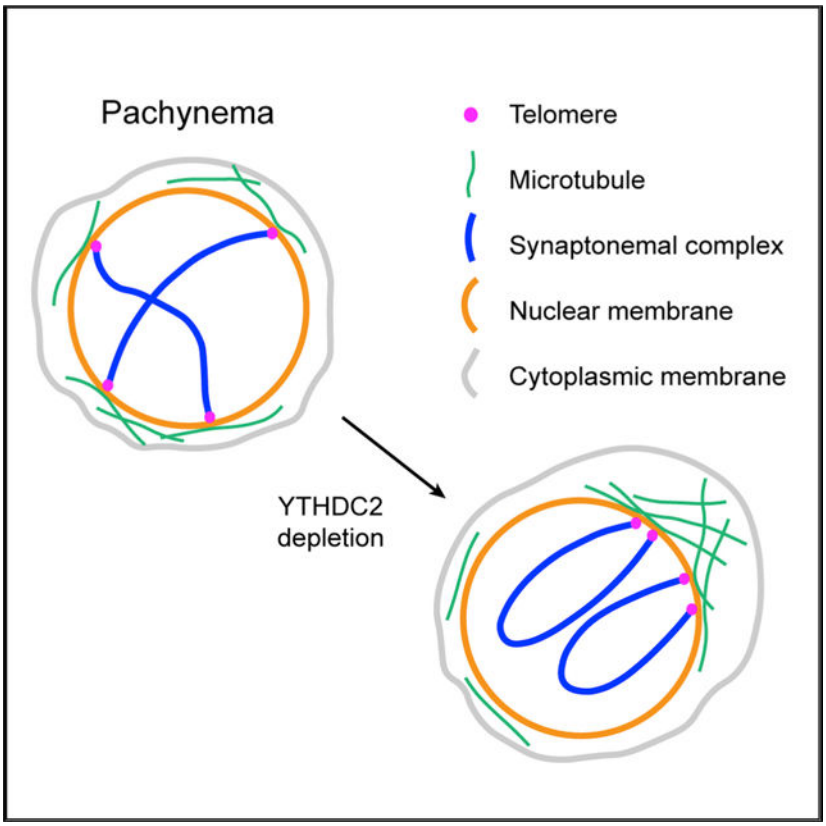

INTRODUCTION

In sexually reproducing organisms, meiosis, a cell cycle program unique to germ cells, leads to production of haploid gametes. Germ cells undergo premeiotic S-phase DNA replication and initiate meiosis. During meiotic prophase I, homologous chromosomes undergo pairing, synapsis, and recombination (Handel and Schimenti, 2010; Zickler and Kleckner, 2015). At the leptotene stage, synaptonemal complex (SC) proteins such as SYCP2 and SYCP3 begin to assemble along chromosomal axes. Homologous chromosomes pair and begin to

synapse, enabled by SC proteins including SYCP1 at the zygotene stage. The pachytene stage is characterized by full synapsis of autosomal homologs and completion of meiotic recombination. Chromosomal desynapsis occurs at the diplotene stage. Meiotic prophase I is generally much longer than mitotic prophase, presumably providing ample time for meiosis-specific chromatin events to complete. In particular, the pachytene stage of meiotic prophase I is the longest, lasting six days in male mice (Russell et al., 1990) and may be required for acquisition of metaphase competence (Guan et al., 2020). However, the temporal maintenance of the prolonged meiotic prophase I remains poorly understood.

N^6-methyladenosine (m^6A) is the most abundant internal modification in eukaryotic transcripts and a critical regulator of RNA stability, splicing, and translation efficiency (Liu and Pan, 2016; Meyer and Jaffrey, 2014; Yue et al., 2015). In mammals, m^6A modification is catalyzed by a heterodimer of METTL3 and METTL14 (Bokar et al., 1997; Liu et al., 2014). IME4, a homolog of METTL3, is an inducer of meiosis and mediates N6-adenosine methylation of bulk mRNA exclusively during sporulation in budding yeast, suggesting an ancient role for the modification in the induction of meiosis (Clancy et al., 2002; Schwartz et al., 2013). The functional outcome of m^6A marks on RNAs is mediated by a family of reader proteins, including YTHdomain-containing proteins: YTHDF1,2,3 and YTHDC1, 2 (Dominissini et al., 2012; Hsu et al., 2017; Wang et al., 2014; Xu et al., 2014; Xu et al., 2015). Crystal structural analyses show that the YTH domain, an RNA-binding motif, utilizes a conserved aromatic cage to accommodate m^6A (Xu et al., 2014; Xu et al., 2015; Zhang et al., 2010). Cells deficient for all three YTHDF proteins accumulate the most m^6A-modified transcripts, showing their combined action on the regulation of mRNA stability (Shi et al., 2017; Zaccara and Jaffrey, 2020).

Unlike other mouse YTH domain m^6A readers (Kasowitz et al., 2018; Lasman et al., 2020), YTHDC2 is specifically required for meiosis (Bailey et al., 2017; Hsu et al., 2017; Jain et al., 2018; Wojtas et al., 2017). *Ythdc2*-deficient germ cells initiate meiosis but prematurely enter a metaphase state with a mixed mitotic and meiotic identity. In addition to the YTH domain, YTHDC2 contains multiple RNA-binding domains including RNA helicase motifs (Figure S1A). YTHDC2 interacts with the 5'→3' exoribonuclease XRN1 through an ankyrin repeat domain (Kretschmer et al., 2018; Wojtas et al., 2017). YTHDC2 also interacts with the small ribosomal subunit (Kretschmer et al., 2018). YTHDC2 is a 3'→5' RNA helicase (Jain et al., 2018; Wojtas et al., 2017). As YTHDC2 recognizes somatic (mitotic) transcripts such as *Ccna2* for degradation upon meiotic entry, the prevailing model is that YTHDC2 modulates the levels of m^6A-modified transcripts in meiotic germ cells to generate a transcriptome that facilitates meiotic progression. YTHDC2 partners with MEIOC, a meiosis-specific protein (Abby et al., 2016; Soh et al., 2017). Strikingly, *Ythdc2*-deficient mouse mutants phenocopy the *Meioc*-deficient mutants.

Intriguingly, the YTHDC2 protein is most abundant in mouse pachytene spermatocytes (Bailey et al., 2017; Jain et al., 2018). However, the early meiotic arrest in all four existing *Ythdc2* global mouse mutants precludes investigation of its putative role at the pachytene stage. To circumvent this hurdle, here we employ an inducible inactivation approach coupled with molecular analyses and demonstrate that YTHDC2 is essential for progression through

the extended pachytene stage by sustaining a meiotic transcriptome and safeguarding against aberrant microtubule-dependent telomere clustering.

RESULTS

Conditional deletion of *Ythdc2* to meiotic blockade at the pachytene stage

YTHDC2 is highly expressed in pachytene spermatocytes (Bailey et al., 2017; Jain et al., 2018). To elucidate a potential role at this later stage in meiotic progression, we generated a *Ythdc2* floxed allele by homologous recombination in ES cells (Figure S1B). In this floxed allele, exons 13–16, encoding the ankyrin repeats and part of the HrpA-like RNA helicase domain, are flanked by *loxP* sites. Cre-mediated removal of exons 13–16 results in a deletion of 149 amino acids (aa 578–726) and a frameshift in the mutant transcript. We first produced $Ythdc2^{-/-}$ (global knockout) mice using the ubiquitous *Actb*-Cre (Lewandoski et al., 1997). $Ythdc2^{-/-}$ males exhibited an early meiotic arrest with metaphase-like spermatocytes, the same phenotype as previously reported (Bailey et al., 2017; Hsu et al., 2017; Jain et al., 2018; Wojtas et al., 2017), showing that this knockout allele is null (Figure S1C). We then conditionally inactivated *Ythdc2* using *Stra8*-Cre, which is primarily expressed in spermatogonia prior to meiotic entry (Figures S1D and S1E) (Baltus et al., 2006; Lin et al., 2017). We also conditionally inactivated *Ythdc2* using the $Ythdc2^{em1}$ allele and *Ngn3*-Cre, which begins to express in spermatogonia at postnatal day 7 (Figures S1F and S1G) (Schonhoff et al., 2004). $Ythdc2^{em1}$ is a deletion allele (Jain et al., 2018). Both $Ythdc2^{fl/-}$ *Stra8*-Cre and $Ythdc2^{fl/em1}$ *Ngn3*-Cre conditional knockout males exhibited a significant reduction in testis size and early meiotic arrest with metaphase-like spermatocytes, which were characterized by heavily condensed chromatin (Figures S1D–S1G). Therefore, the newly generated *Ythdc2* global knockout and two *Ythdc2* conditional knockout mouse mutants exhibited meiotic defects that were similar to the phenotypes of the previously reported $Ythdc2^{-/-}$mutants.

To circumvent the early meiotic block in both global and conditional knockout *Ythdc2* mutants, we generated $Ythdc2^{fl/-}$ *Ddx4*-Cre^{ERT2} mice (referred to as $Ythdc2^{iKO}$) for tamoxifen-inducible deletion in germ cells (Figure 1A). *Ddx4*-Cre^{ERT2} is expressed in both mitotic and meiotic germ cells (John et al., 2008). Intraperitoneal tamoxifen injection of adult $Ythdc2^{iKO}$ males revealed a progressive decrease in testis weight after treatment (Figure 1B). The abundance of YTHDC2 in $Ythdc2^{iKO}$ testes was reduced at 2 days post tamoxifen treatment (2 dpt) and decreased sharply over time (Figure 1C). Histological analysis showed progressively severe spermatogenic defects in $Ythdc2^{iKO}$ testes (Figure 1D). Spermatogenesis occurs in waves, and seminiferous tubules are sequentially divided into twelve stages, each of which is defined by a specific cohort of spermatogonia, spermatocytes, and spermatids. Each stage on average lasts about 20 hours in mice (Russell et al., 1990). At 2 dpt, apoptotic pachytene spermatocytes were observed in $Ythdc2^{iKO}$ seminiferous tubules (one cell layer away from the basement membrane). Strikingly, these abnormal pachytene cells were present in stages VIII, IX, and X (Figure 1D), but not in early-stage tubules (I–VII) (data not shown), and thus were late pachytene cells. In 4 and 6 dpt $Ythdc2^{iKO}$ seminiferous tubules, abnormal pachytene cells were still present but pachytene cells were severely depleted in stages VIII–X (Figure S2). In 8 and 10 dpt

Ythdc2^{iKO} tubules, pachytene spermatocytes were absent (Figure S2). These results revealed a progressive loss of spermatocytes with time after the last tamoxifen injection (Figure S2). Notably, round and/or elongated spermatids from the previous wave of spermatogenesis were still present in *Ythdc2*^{iKO} tubules, further supporting a block in meiotic progression in the current wave.

We examined chromosomal synapsis and meiotic recombination in spermatocytes from adult testes by immunofluorescent analysis of SYCP1 (a component of the synaptonemal complex transverse filaments), SYCP2 (a component of lateral elements), and γH2AX (Figure 1E). *Ythdc2*^{iKO} pachytene cells displayed normal synapsis as shown by the colocalization of SYCP1 and SYCP2 on all homologs except XY. Meiotic DNA double strand breaks were apparently repaired, since γH2AX was absent on autosomes and restricted to the XY body in *Ythdc2*^{iKO} pachytene cells (Figure 1E).

We next determined the composition of prophase I spermatocytes in adult testes. The control adult testis contained a full spectrum of prophase I spermatocytes from leptotene to diakinesis (Figure 1E and 1F). However, the *Ythdc2*^{iKO} testes contained leptotene, zygotene, and pachytene cells, but were depleted of diplotene cells at 2, 4, and 6 dpt (Figures 1E and 1F). Diplotene spermatocytes are present in stage XI tubules in control, however, histology of *Ythdc2*^{iKO} testes revealed a loss of diplotene spermatocytes at stage XI (Figure 1D and Figure S2). Diakinesis/metaphase I spermatocytes were still present in stage XII tubules from *Ythdc2*^{iKO} testes at 2 dpt (presumably from the previous wave of spermatogenesis) (Figure 1G) but were absent at 4 dpt and beyond (Figure S2B). These results demonstrate that YTHDC2 is required for progression through the pachytene stage of meiotic prophase I.

Depletion of YTHDC2 causes telomere clustering at the pachytene stage

Meiotic chromosome telomeres are attached to the nuclear membrane by the meiotic telomere complex (Shibuya et al., 2015) and connected to the cytoplasmic cytoskeleton network through the LINC complex (Ding et al., 2007; Starr and Han, 2002). In wild-type meiotic cells, telomeres are transiently clustered in a phenomenon termed *bouquet formation* at the zygotene stage, but this clustering no longer occurs during the pachytene stage (Scherthan, 2001; Zickler and Kleckner, 1998). The bouquet stage of wild-type mouse zygotene spermatocytes was previously shown (Pandita et al., 1999). Bouquet formation has been proposed to facilitate homolog search and pairing during meiosis. Unexpectedly, we observed pronounced telomere clustering (termed 'TC') as a polarized configuration in pachytene cells from *Ythdc2*^{iKO} testis but not from control testis (Figure 1E). Such abnormal pachytene cells accounted for > 20% of prophase I spermatocytes (Figure 1E). In TC pachytene cells, the synaptonemal complexes formed U-shaped loops that had low staining intensity for SC proteins and that appeared to be elongated relative to normal pachytene chromosomes (Figure 1E).

We confirmed telomere clustering in *Ythdc2*^{iKO} pachytene cells with immunofluorescence of CREST (centromere marker) and SUN1 (LINC telomere marker) (Figure 2A) (Crisp et al., 2006; Ding et al., 2007). Mouse chromosomes are acrocentric (i.e., with the centromere positioned at one end). Immunofluorescence of SUN1 in intact *Ythdc2*^{iKO} pachytene cells further confirmed telomere clustering (Figure 2B). Confocal microscopy of CREST

and SYCP3 showed that centromeres were randomly distributed in *Ythdc2*$^{fl/-}$ pachytene cells (Video S1) but congregated to one side of the nucleus in *Ythdc2*^{iKO} pachytene cells (Video S2). To determine when telomeres cluster during the pachytene stage, H1t immunofluorescence was performed. H1t is expressed in mid to late pachytene cells but not early pachytene cells (Figure 2C) (Cobb et al., 1999). *Ythdc2*^{iKO} pachytene cells with telomere clustering were H1t-positive and thus were at the mid-late pachytene stage (Figure 2C). In 2 dpt *Ythdc2*^{iKO} testes, early pachytene cells lacked telomere clustering, nearly half of mid pachytene cells displayed telomere clustering, and most late pachytene cells exhibited telomere clustering (Figure 2D). These results show that *Ythdc2*^{iKO} spermatocytes develop telomere clustering at the mid-late pachytene stage.

Elimination of *Ythdc2*^{iKO} spermatocytes at the pachytene stage

The depletion of diplotene cells in *Ythdc2*^{iKO} testes (Figure 1E) implies that *Ythdc2*^{iKO} pachytene cells die at a specific stage. The pachytene stage of male meiosis is unusually long, spanning 6 days in mice. To pinpoint the timing of spermatocyte death in *Ythdc2*^{iKO} testes, we performed TUNEL analysis coupled with precise staging of seminiferous tubules (Figure 3). We observed sharply increased apoptosis in *Ythdc2*^{iKO} testes at 2 dpt compared with controls. The occurrence of apoptosis in *Ythdc2*^{iKO} testes was stage-dependent. Tubules at stages VIII, IX, and X displayed the highest percentage (> 80%) of tubules with TUNEL-positive cells (Figures 3A and 3B). Stages VIII–X contained late pachytene cells (located one cell layer away from the basement membrane) and preleptotene cells (VIII) or leptotene cells (IX and X) (the outermost layer of germ cells) (Figure 3A). Because TUNEL-positive cells in stages VIII–X *Ythdc2*^{iKO} tubules were located one cell layer away from the basement membrane and contained thread-like chromatin (a characteristic of pachytene cells), these apoptotic spermatocytes were late pachytene cells (Figure 3A). Quantification of apoptotic cells in all 12 stages revealed that the level of apoptosis in *Ythdc2*^{iKO} testes at 2 dpt increased significantly at stage VIII and peaked at stages IX and X, whereas the level of apoptosis at stages I–VII and XII remained low in *Ythdc2*^{iKO} testes, similar to control (Figure 3C). In addition, increased apoptosis occurred in *Ythdc2*^{iKO} testes at 4 and 6 dpt (data not shown). These results demonstrate that mutant spermatocytes are specifically eliminated by apoptosis at the late pachytene stage, resulting in the absence of diplotene cells in *Ythdc2*^{iKO} testis.

Ythdc2^{iKO} leptotene cells prematurely condense chromatin

Male germ cells (preleptotene cells) in *Ythdc2*-deficient mice initiate meiosis and enter prematurely into a mitotic-metaphase-like state with condensed chromatin (Bailey et al., 2017; Hsu et al., 2017; Jain et al., 2018; Wojtas et al., 2017). To investigate whether this is the case for *Ythdc2*^{iKO} male germ cells, we performed immunofluorescence analysis of pH3 (phosphorylated histone H3 at serine 10), which is a metaphase marker (Sun and Handel, 2008). In control testis, metaphase I/II spermatocytes (pH3-positive) were only present at stage XII tubules (Figure S3A). Likewise, in 2 dpt *Ythdc2*^{iKO} testis, most pH3-positive spermatocytes were observed at stage XII, and the preleptotene (stage VIII) and leptotene (stages IX and X) were pH3-negative (Figures S3A and S3B). Strikingly, in 4 dpt *Ythdc2*^{iKO} testis, the outermost layer of germ cells at stages VIII, IX, and X were pH3-positive and exhibited condensed chromatin, indicating a metaphase-like state (Figure

S3A). Quantification of pH3-positive cells showed the highest number of pH3-positive cells at stage-IX tubules from 4 dpt *Ythdc2*^{iKO} testis (Figure S3C). In addition, 6 dpt *Ythdc2*^{iKO} testis contained pH3-positive metaphase-like germ cells at stages VIII, IX, and X (Figure S3A). Consistently, histological analyses showed that leptotene cells and zygotene cells were present in *Ythdc2*^{iKO} tubules at 2 dpt and 4 dpt, but severely depleted at 6 dpt (Figure S2). Furthermore, zygotene cells were absent in stage-XI/XII *Ythdc2*^{iKO} tubules at 8 and 10 dpt (Figure S2). These results demonstrate that *Ythdc2*^{iKO} male germ cells enter meiosis but fail to progress through the leptotene stage and prematurely condense chromatin in a metaphase-like state. Therefore, these results pinpoint the requirement of YTHDC2 at the leptotene and zygotene stages in agreement with the global deletion.

Ythdc2^{iKO} pachytene cells with telomere clustering are metaphase-competent

Okadaic acid, an inhibitor of protein phosphatases PP1 and PP2A, induces progression of pachytene cells into metaphase I *in vitro* (Wiltshire et al., 1995). *Ythdc2*^{iKO} pachytene cells failed to progress to the diplotene stage in the testis. To address whether *Ythdc2*^{iKO} pachytene cells with telomere clustering are competent for metaphase I entry, spermatocytes were treated with okadaic acid in culture (Figure 4A). Among both control (*Ythdc2*$^{fl/-}$) and *Ythdc2*^{iKO} spermatocytes, the percentage of diakinesis/metaphase I spermatocytes increased to over 80% after OA treatment (Figure 4B). Accordingly, the percentage of *Ythdc2*^{iKO} pachytene cells with telomere clustering was sharply reduced. These results demonstrate that *Ythdc2*^{iKO} pachytene cells are competent for entry into metaphase I.

Massively altered transcriptome in *Ythdc2*^{iKO} pachytene cells

To elucidate the molecular defects in *Ythdc2*^{iKO} pachytene spermatocytes, we performed RNA-seq analysis. Because whole testes contained both somatic and germ cells and differed in cellular composition between control and mutant, pachytene cells were purified by the Sta-put method and used for RNA-seq analysis (Figure S4A). Abnormal TC pachytene spermatocytes were present in the Sta-put purified *Ythdc2*^{iKO} pachytene population (Figure S4A). A large number of differentially expressed genes were identified between *Ythdc2*$^{fl/-}$ (control) and *Ythdc2*^{iKO} pachytene cells at 2 dpt (Figure 5A). With the cutoff of $\log_2$ (Fold Change) ≥ 0.5 or ≥ -0.5, RNA-seq analysis revealed more upregulated genes (3,147 genes) than downregulated genes (1,812 genes) in *Ythdc2*^{iKO} pachytene cells (Figure 5B; Table S1). The expression changes of a set of 16 differentially expressed genes (8 upregulated and 8 downregulated) were validated and confirmed by qPCR (Figures S4B and S4C). Western blot analysis of purified pachytene cells showed that the abundance of YTHDC2 was reduced in *Ythdc2*^{iKO} pachytene cells, as expected (Figure S4D). Consistent with the downregulation of its transcript, SYCP2 protein abundance was reduced in *Ythdc2*^{iKO} pachytene cells (Figure S4D). Even though the *Meioc* transcript was significantly increased in the *Ythdc2*^{iKO} cells, the abundance of MEIOC protein remained constant (Figure S4D), potentially because the reduced abundance of its binding partner YTHDC2 in *Ythdc2*^{iKO} cells led to its instability (Figure S5A).

The top enriched GO terms for upregulated genes are *actin binding*, *focal adhesion*, *regulation of signal transduction*, and *regulation of apoptosis* (Figure S5B). The top enriched GO terms for downregulated genes are *RNA-binding*, *microtubule organizing center*, and

cilium assembly and organization (Figure S5C). We next examined the expression profile of differentially expressed genes among specific spermatogenic populations: spermatogonia (mitotic), spermatocytes (meiotic), and round spermatids (post-meiotic), using the germ cell RNA-seq data (Davis et al., 2017). The upregulated genes in *Ythdc2*^{iKO} pachytene cells exhibit higher expression levels in spermatogonia than spermatocytes, suggesting that YTHDC2 promotes degradation of mitotic transcripts in spermatocytes (Figure 5C). In contrast, the downregulated genes normally show higher expression levels in spermatocytes (Figure 5C).

Notably, the overall transcript levels of X chromosome-linked genes and mitochondria-encoded genes were upregulated in *Ythdc2*^{iKO} pachytene cells (Figure S5D). Although all autosomes had both upregulated and downregulated genes, all differentially expressed X-linked genes (274 genes) were upregulated (Figure S5E). XY chromosomes undergo MSCI (meiotic sex chromatin inactivation) in male meiosis (Turner, 2015). We performed immunofluorescence of RNA polymerase II to examine MSCI. As expected, RNA polymerase II was excluded from the XY body in *Ythdc2*$^{fl/-}$ (control) late pachytene spermatocytes (Figure S6). This was also the case in *Ythdc2*^{iKO} late pachytene spermatocytes with telomere clustering, suggesting that MSCI appeared to be intact in *Ythdc2*^{iKO} pachytene spermatocytes (Figure S6).

YTHDC2 destabilizes its target transcripts

YTHDC2-bound transcripts are enriched for the m^{6}A modification (Bailey et al., 2017; Hsu et al., 2017; Wojtas et al., 2017). We analyzed the *Ythdc2*^{iKO} expression changes among genes known to be enriched or depleted of m^{6}A (Wojtas et al., 2017), but found no correlation between expression changes in *Ythdc2*^{iKO} pachytene cells and the level of m^{6}A in mRNAs (Figure 5D). This could indicate that the m^{6}A-binding activity of YTHDC2 is dispensable or that these expression changes are mostly indirect effects.

YTHDC2 contains multiple RNA-binding domains: YTH, R3H, and RNA helicase domain (Figure S1A) (Jain et al., 2018; Kretschmer et al., 2018; Wojtas et al., 2017). YTHDC2 lacking the YTH domain still binds to cellular RNAs (Kretschmer et al., 2018). The target mRNAs of YTHDC2 in testes were previously identified by RNA immunoprecipitation sequencing (RIP-seq) and 521 YTHDC2 target mRNAs were reported (Hsu et al., 2017). Out of these 521 genes, 148 genes (28%) were upregulated, but only 32 genes (6%) were downregulated in *Ythdc2*^{iKO} pachytene cells (Figure 5E and Table S2). Out of 80 YTHDC2 target transcripts reported in another study (Soh et al., 2017), 21 genes (26%) were upregulated but only one was downregulated in *Ythdc2*^{iKO} pachytene cells (Figure 5F and Table S2). Both *Pbrm1* and *Rad21* are YTHDC2 target transcripts identified by RIP-seq (Table S2) and are upregulated in *Ythdc2*^{iKO} pachytene cells (Table S1). PBRM1 is a component of the PBAF chromatin-remodeling complex (Brownlee et al., 2014) and RAD21 is a mitotic/meiotic cohesin (Xu et al., 2004). The protein abundance of PBRM1 and RAD21 was increased in *Ythdc2*^{iKO} pachytene cells (Figure S4D). In conclusion, the preferential upregulation of YTHDC2 target transcripts in *Ythdc2*^{iKO} pachytene cells further supports that YTHDC2 primarily targets transcripts for degradation. However, we could not exclude the possibility that differential expression of some DEGs might be attributed

to the subtle differences between control and *Ythdc2*^{iKO} purified pachytene populations. In addition, given that only about one-third of YTHDC2 RIP targets were differentially expressed (Figure 5E), many DEGs could be attributed to secondary effects of YTHDC2 depletion.

Microtubule-dependent telomere clustering in *Ythdc2*^{iKO} pachytene cells

The top GO terms of downregulated genes in *Ythdc2*^{iKO} pachytene cells are related to microtubules: *microtubule organizing center*, *centriole*, and *cilium* (Figure S5C). Even though microtubule-related categories are not among the top 10 GO terms for upregulated genes (Figure S5B), 39 upregulated genes encode tubulins, microtubule-associated proteins, dyneins, and kinesins (Table S1). We closely examined the 148 upregulated DEGs that are present in the YTHDC2 RIP target dataset (Figure 5E and Table S2) (Hsu et al., 2017). Five of them encode microtubule-associated or crosslinking proteins: *Map1b*, *Map9*, *Macf1*, *Mtcl1*, and *Eml5* (Table S2). Microtubule dynamics is tightly regulated by microtubule-associated proteins. In mammalian cells, telomere-led meiotic chromosome movement is primarily driven by cytoplasmic microtubule-based forces (Lee et al., 2015). It is possible that upregulation of microtubule-associated proteins contributes to telomere clustering in *Ythdc2*^{iKO} spermatocytes. To address whether the microtubule cytoskeleton is responsible for abnormal telomere clustering, we examined the microtubule network in intact pachytene cells. In *Ythdc2*$^{fl/-}$ pachytene cells, cytoplasmic microtubules were randomly distributed and telomeres (indicated by SUN1) were distributed throughout the nuclear periphery (Figure 6A). Strikingly, in 83% of *Ythdc2*^{iKO} pachytene cells with clustered telomeres (83% ± 8%; 82 TC pachytene cells from three males were analyzed), microtubules converged to the region where telomeres were clustered (Figure 6A). In addition, the side where both microtubules and telomeres congregated expanded cytoplasm (Figure S7). The cytoplasmic expansion is likely associated with aggregation of the microtubule cytoskeleton (Figure S7). These results suggest that telomere clustering could be attributed to the polarized distribution of cytoplasmic microtubules in *Ythdc2*^{iKO} pachytene cells.

To further test the role of microtubules in telomere clustering, *Ythdc2*^{iKO} germ cells were treated with nocodazole, an inhibitor of microtubule polymerization (Figure 6B). The percentage of *Ythdc2*^{iKO} pachytene cells with telomere clustering was significantly reduced from 24.2% (24.2% ± 6.9%, n = 3, $p < 0.01$) in DMSO treatment to 4.8% (4.8% ± 1.3%) in nocodazole treatment (Figure 6C). The percentage of metaphase I spermatocytes was significantly increased in nocodazole-treated *Ythdc2*^{iKO} spermatocytes (Figure 6C). The percentage of normal-looking *Ythdc2*^{iKO} pachytene cells was also increased upon nocodazole treatment, although the difference was not statistically significant (Figure 6C). These results suggest that nocodazole treatment causes *Ythdc2*^{iKO} TC pachytene cells to progress further to metaphase I stage or resolve telomere clustering to become normal-looking pachytene cells. Treatment of *Ythdc2*^{iKO} cells with colcemid, another microtubule inhibitor, also reduced the percentage of pachytene cells with telomere clustering (data not shown). The top GO terms of the upregulated genes in *Ythdc2*^{iKO} pachytene cells are related to actin: *actin-binding* and *focal adhesion* (Figure S5B). However, treatment with actin inhibitors (latrunculin A and cytochalasin D) did not significantly affect the percentage of *Ythdc2*^{iKO} pachytene cells with telomere clustering (Figure S8). Collectively, these results

demonstrate that inhibition of microtubule but not actin polymerization rescues abnormal telomere clustering in *Ythdc2*^{iKO} pachytene cells.

DISCUSSION

All previous studies of *Ythdc2* global knockout mice report a requirement for YTHDC2 around the point of meiotic entry (Figure 7A) (Bailey et al., 2017; Hsu et al., 2017; Jain et al., 2018; Wojtas et al., 2017). In this study, we employed an inducible inactivation approach and uncovered an additional function for YTHDC2 in meiosis—progression through the extended pachytene stage during meiotic prophase I. This finding is consistent with the fact that YTHDC2 is most abundant in pachytene cells. Therefore, YTHDC2 plays essential roles at two distinct stages of meiotic prophase I: at the time of meiotic entry and during late pachytene (Figure 7A). At the early point, YTHDC2-deficient spermatocytes fail to downregulate mitotic genes such as *Ccna2* and undergo chromatin condensation with mixed mitotic/meiotic characteristics (Bailey et al., 2017; Hsu et al., 2017; Jain et al., 2018; Wojtas et al., 2017). Our *Ythdc2*^{iKO} study confirms the requirement for YTHDC2 at this early stage and, furthermore, pinpoints the time of chromatin condensation (pH3-positivity) to seminiferous tubule stages VIII–IX, which is the time when spermatocytes would normally be in preleptotene and leptotene stages. Thus, YTHDC2 is necessary for progression into normal leptotene. At the pachytene stage, depletion of YTHDC2 causes a massively dysregulated transcriptome. *Ythdc2*^{iKO} pachytene cells are arrested at the late pachytene stage and fail to progress to the diplotene stage. Unlike *Ythdc2*-deficient leptotene cells, *Ythdc2*^{iKO} pachytene cells are pH3-negative and do not undergo chromatin condensation, suggesting that pachytene cells have irreversibly committed to the meiotic program.

Defects in chromosomal synapsis and/or meiotic recombination lead to mid-pachytene arrest at stage IV in males, presumably due to a pachytene checkpoint (de Rooij and de Boer, 2003). Although the pachytene checkpoint in yeast is well known (Roeder and Bailis, 2000), components of the pachytene checkpoint in mice have not been identified. XY chromosomes undergo MSCI during meiosis (Turner, 2015), and genetic studies demonstrate that an MSCI checkpoint operates at stage IV (Abe et al., 2020; Royo et al., 2010). In early pachytene cells, DNA damage repair factors are redistributed from autosomes to XY to achieve MSCI (Abe et al., 2020). Ectopic expression of two Y-linked genes *Zfy1* and *Zfy2* is sufficient to cause death of pachytene spermatocytes at stage IV, suggesting that escape of *Zfy1/2* from MSCI contributes mechanistically to the MSCI checkpoint (Royo et al., 2010). In this study, we report the death of *Ythdc2*^{iKO} meiotic cells at the late pachytene stage (VIII–X). The late pachytene apoptosis of *Ythdc2*^{iKO} meiotic cells could be due to the dramatically altered transcriptome in *Ythdc2*^{iKO} pachytene cells or due to the existence of a late pachytene checkpoint. The transcript levels of *Zfy1* and *Zfy2* remain unchanged in *Ythdc2*^{iKO} pachytene cells and thus are not responsible for apoptosis. However, 274 X-linked genes were upregulated, but none were downregulated in *Ythdc2*^{iKO} pachytene cells; and *Zfx*, the X-linked paralog of *Zfy1/2* (Luoh et al., 1997), was upregulated in *Ythdc2*^{iKO} pachytene cells (Table S1). Thus, it is possible that overexpression of X-linked genes such as *Zfx* might be lethal to late pachytene cells.

Telomeres are connected to the cytoplasmic cytoskeleton network through the SUN/KASH proteins (Crisp et al., 2006; Starr and Han, 2002). The SUN domain proteins are located at the inner nuclear membrane and interact with telomere-associated proteins. The KASH domain proteins are outer nuclear membrane components and are associated with the cytoplasmic cytoskeleton (Starr and Han, 2003). In both somatic and germ cells, chromosome migration and positioning are driven by cytoskeletal forces through the SUN/KASH proteins. A meiosis-specific telomere cap protein complex (MAJIN, TERB1, and TERB2) links telomeres to the nuclear envelope through the SUN domain proteins (Shibuya et al., 2015). Telomere clustering (the so-called bouquet formation) occurs only in zygotene cells in wild-type (Scherthan, 2001). In budding yeast, meiotic chromosome movement is driven by actin cytoskeleton but not microtubules (Conrad et al., 2008; Koszul et al., 2008; Trelles-Sticken et al., 2005). Telomere-led rapid chromosome movement also occurs in pachytene cells and its function is likely to resolve chromosome entanglements (Lee et al., 2015). In mouse pachytene cells, chromosome movement depends on cytoplasmic microtubules and dynein motor proteins (Lee et al., 2015). Unexpectedly, *Ythdc2*^{iKO} cells exhibit abnormal telomere clustering at the late pachytene stage. This defect is caused by dysregulated cytoplasmic microtubule network but not actin cytoskeleton (Figure 7B). This conclusion is supported by three lines of evidence. First, a large number of differentially expressed (both upregulated and downregulated) genes in *Ythdc2*^{iKO} pachytene cells encode tubulins, microtubule-associated proteins, dyneins, and kinesins (Table S1). Second, cytoplasmic microtubules and telomeres converge to the same pole in *Ythdc2*^{iKO} pachytene cells where the cytoplasm is expanded. This observation supports a direct connection between polarized microtubule networks and telomere clustering. Finally, telomere clustering in *Ythdc2*^{iKO} cells can be resolved by treatment with inhibitors of microtubules but not actin filaments.

YTHDC2 is an obligate binding partner of MEIOC, and *Ythdc2* global knockout mutants phenocopies *Meioc* global knockout mutants (Abby et al., 2016; Bailey et al., 2017; Hsu et al., 2017; Jain et al., 2018; Soh et al., 2017; Wojtas et al., 2017). Like YTHDC2, MEIOC is abundantly expressed in pachytene cells (Abby et al., 2016; Soh et al., 2017). Notably, the *Meioc* global knockout mutants exhibit telomere clustering in zygotene-like spermatocytes (Abby et al., 2016). Therefore, we postulate that inducible inactivation of MEIOC is likely to cause the same defects as *Ythdc2*^{iKO}: abnormal telomere clustering in pachytene cells and meiotic arrest at the late pachytene stage. MEIOC lacks known RNA-binding domains and thus the exact mechanism of MEIOC function is unknown. YTHDC2 interacts with XRN1, a 5'→3' exoribonuclease, which participates in degradation of cellular transcripts (Kretschmer et al., 2018; Wojtas et al., 2017). The YTHDC2/MEIOC complex has been proposed to target its mitotic substrate transcripts for degradation (Soh et al., 2017; Wojtas et al., 2017). In support of the RNA degradation model, the reported YTHDC2 target transcripts are preferentially upregulated in *Ythdc2*^{iKO} pachytene cells. In addition, we find that differential gene expression in *Ythdc2*^{iKO} pachytene cells does not correlate with the m^{6}A RNA modification, suggesting that YTHDC2 might modulate the transcriptome independently of the m^{6}A modification. In conclusion, our study demonstrates that YTHDC2, and presumably MEIOC as well, continue to be required for actively

maintaining a meiotic transcriptome at the prolonged pachytene stage of meiotic prophase I long after meiotic entry.

Limitations of the study

Because the *Ythdc2*^{iKO} meiotic germ cells exhibited defects at the pachytene stage, we performed RNA-seq analysis of pachytene cells isolated using the STA-PUT method. Use of isolated wild-type and *Ythdc2*^{iKO} pachytene populations has obvious advantages over the use of whole adult testes, which contained other cell types and differed in cellular compositions. However, the pachytene stage lasts for 6 days in male mice (Russell et al., 1990) and thus the early, mid, and late pachytene cells may differ in their transcriptomes. The STA-PUT method isolates all pachytene cells. The *Ythdc2*^{iKO} pachytene population might be skewed toward early-mid pachytene cells in comparison with the wild-type pachytene population. Therefore, it is possible that differential expression of some DEGs might be due to subtle differences in cellular composition between *Ythdc2*^{iKO} and wild-type pachytene populations. Our analysis was complicated by the lack of overlap among YTHDC2 mRNA targets reported in different studies (Hsu et al., 2017; Soh et al., 2017). However, our data have shown that 26% to 28% of reported YTHDC2 RIP targets are differentially expressed (Figures 5E and 5F), suggesting a direct effect of YTHDC2 on the stability of these transcripts.

STAR * METHODS

RESOURCE AVAILABILITY

Lead contact—Further information and requests for resources and reagents should be directed to and will be fulfilled by the Lead Contact, P. Jeremy Wang (pwang@upenn.edu).

Materials availability—*Ythdc2* mutant mice and all unique materials are available from the lead contact.

Data and code availability—All data reported in this paper will be shared by the lead contact upon request. The RNA-seq data have been deposited in Gene Expression Omnibus with the accession number GEO: GSE166568. This paper does not report original code. Any additional information required to reanalyze the data reported in this paper is available from the lead contact upon request.

EXPERIMENTAL MODEL AND SUBJECT DETAILS

Mouse strains—All mice were maintained on a hybrid genetic background (C57BL/6 × 129S4/SvJae × FVB/N). The *Ythdc2* floxed allele was initially generated on the C57BL/6 × 129S4/SvJae hybrid background. The *Ddx4*-Cre^{ERT2} mouse strain was on the FVB/N genetic background. In all cases, experiments were performed on tissues from adult male mice between the ages of 8 and 12 weeks. All mice were maintained in a specific pathogen–free facility and used under protocol (Protocol number 804421) approved by the University of Pennsylvania Institutional Animal Care and Use Committee and in accordance with National Institutes of Health (NIH) guidelines.

Generation of *Ythdc2* mutant mice—The *Ythdc2* targeting construct was designed to insert a *loxP*-flanked hygromycin phosphotransferase-thymidine kinase (HyTK) drug selection cassette into *Ythdc2* intron 12, and a *loxP* site into intron 16 (Figure S1A). Genomic fragments were amplified from the *Ythdc2*-containing BAC clone RP23–138L17 by PCR with high-fidelity Taq DNA polymerase (BD Biosciences). The targeting construct was confirmed by sequencing. *FspI*-linearized targeting construct was electroporated into V6.5 mouse embryonic stem (ES) cells (on a C57BL/6 × 129S4/SvJae hybrid background) (Eggan et al., 2001), and ES cells were cultured in media containing 120 μg/ml hygromycin B (Invitrogen). Of 92 hygromycin-resistant ES clones screened by long-range PCR, one clone (C4) was homologously targeted. Clone C4 was expanded and electroporated with *Cre*-expressing plasmid pOG231, followed by culture in media containing 2 μM ganciclovir. Ninety-two clones were screened for removal of the HyTK cassette and presence of *loxP* sites flanking *Ythdc2* exons 13–16, resulting in nine positive clones ($Ythdc2^{fl/+}$). Two (C4B9 and C4H7) $Ythdc2^{fl/+}$ ES clones were injected into blastocysts. The resulting chimeric male mice transmitted the *Ythdc2* floxed allele through the germline by breeding with C57BL/6 females.

Ythdc2 floxed mice were crossed with four different Cre strains: *Actb*-Cre (Lewandoski et al., 1997), *Stra8*-Cre (Lin et al., 2017), *Neurog3*-Cre (Schonhoff et al., 2004), and *Ddx4*-Cre^{ERT2} (on the FVB/N genetic background) (John et al., 2008). *Ddx4*-Cre^{ERT2} is tamoxifen-inducible Cre and expressed throughout spermatogenesis, including spermatogonia, spermatocytes, and round spermatids (John et al., 2008). Tamoxifen injection induces Cre-mediated deletion of exons 13–16 (Figure S1A). As described previously (Guan et al., 2020; Shi et al., 2019), tamoxifen (Sigma) was suspended with corn oil (Sigma) and injected intraperitoneally daily into the ≥ 8-week-old $Ythdc2^{fl/-}$ *Ddx4*-Cre^{ERT2} males (2 mg/30 g body weight) for five consecutive days. $Ythdc2^{fl/-}$ males (no Cre) injected with tamoxifen were used as controls. Testes were collected for analysis at 2, 4, 6, 8, and 10 days post-tamoxifen treatment. *Ythdc2* wild-type (473 bp) and floxed (396 bp) alleles were assayed with primers GATGGGCCATATTCCACTTG and TGCTGCTGTTGGCTTTTATG. $Ythdc2^{-}$ (deletion) allele (426 bp) was assayed with primers GCCAGTGTTCCAAAATTGCT and TGCTGCTGTTGGCTTTTATG. *Ddx4*-Cre^{ERT2} allele (205 bp) was assayed with primers ATACCGGAGATCATGCAAGC and GGCCAGGCTGTTCTTCTTAG. Previous studies of *Rpa1*, *Skp1*, and *Chek1* using *Ddx4*-Cre^{ERT2} coupled with tamoxifen injection did not show telomere clustering defects in pachytene spermatocytes as observed in $Ythdc2^{iKO}$ testes (Abe et al., 2018; Guan et al., 2020; Shi et al., 2019). In addition, tamoxifen treatment of adult *Ddx4*-Cre^{ERT2} mice did not cause meiotic defects (Abe et al., 2018).

METHOD DETAILS

Histology, TUNEL, immunofluorescence, and nuclear spread analyses—For histological analysis, testes were fixed in Bouin's solution at room temperature overnight, embedded in paraffin and sectioned in 6 μm. Sections were stained with hematoxylin and eosin (Fisher Scientific). For TUNEL and immunofluorescence assays, testes were fixed in 4% paraformaldehyde (in 1 × PBS) at 4°C overnight, dehydrated in 15% sucrose (in 1 × PBS) for 3 hours, and finally in 30% sucrose (in 1× PBS) overnight. Dehydrated

testes were embedded in Optimal Cutting Temperature compound (OCT) and cut in 6-μm sections on a cryostat. Alternatively, for TUNEL and immunofluorescence assays, testes were fixed in the modified Davidson's fixative solution (30% of a 37%–40% formaldehyde solution, 15% ethanol, and 5% glacial acetic acid) overnight, embedded in paraffin, and cut in 6-μm sections on a microtome. After deparaffinization and rehydration, slides were immersed in the antigen retrieval buffer (10 mM sodium citrate buffer, 0.05% Tween-20, pH 6.0) at 95°C for 20 minutes (Slides used for TUNEL assay were not processed by heat-induced antigen retrieval). For permeation treatment, slides were incubated in 0.5% Triton X-100 in 1 × PBS at room temperature for 10 minutes. The slides were then blocked with 10% goat serum in PBST at 37°C for 1 hour followed by incubating with anti-SP10 antibodies at 37°C overnight. The morphology of acrosome revealed by anti-SP10 (ACRV1) antibody was used to precisely identify stages of seminiferous tubules. Slides were rinsed with PBS containing 0.1% tween-20 and then incubated with goat anti-rabbit, goat anti-mouse, or goat anti-guinea pig secondary antibodies (Vector Lab) at 37°C for 1h. Mounting medium with DAPI was added to the slides for imaging. For surface nuclear spread analysis, spermatocytes from 2, 4 and 6 dpt testes as well as the control were used according to the method described elsewhere (Dia et al., 2017; Peters et al., 1997) with minor modifications. Briefly, testicular tubules were separated from testis after removing the tunica albuginea and soaked in nuclear extraction hypotonic buffer (30 mM Tris, 50 mM Sucrose, 17 mM Trisodium Citrate Dihydrate, 5 mM EDTA, 0.5 mM dithiothreitol (DTT), 1 mM phenylme-thylsulfonyl fluoride (PMSF)). Cells were released by grinding with tweezers and suspended in 100 mM sucrose, and were then spread on a thin layer of paraformaldehyde solution containing Triton X-100 on slides. The primary antibodies used for immunofluorescence analyses are listed in Key Resources Table.

Imaging analysis—Histological images were captured on the Leica DM5500B microscope with a DFC450 digital camera (Leica Microsystems). Most immunolabeled chromosome spread images were taken on a Leica DM5500B microscope with an ORCA Flash4.0 digital monochrome camera (Hamamatsu Photonics). Images were processed using Adobe Photoshop CS6 and ImageJ v1.52p software packages (NIH, USA). Confocal images were acquired on a Leica SP5 confocal system with a 100× (1.46 NA) objective lens and processed with Huygens Essential deconvolution software (Scientific Volume Imaging). For supplemental movies, surface 3D renderings were created with Imaris software (Bitplane) and rotation sequences exported.

YTHDC2 antibody production—Recombinant 6 × His-YTHDC2 fusion protein (residues 1 to 239; mouse YTHDC2 protein accession number, NP_001156485.1) was expressed in *E. coli* BL21 cells using the pQE30 vector. The cDNA fragment encoding the N-terminal 239 aa of mouse YTHDC2 was amplified by PCR from the *Ythdc2* plasmid (NM_001163013) (Cat. No. MR226474, OriGene Technologies) using these two primers: 5'-CGCGGATCCATGTCCAGGCCGAGCAG-3' and 5'-CCCAAGCTTTGTGGTCTTTCCAGACCCAGT-3', and was cloned into the BamHI and HindIII sites of the pQE30 vector. The purified 6 × His-YTHDC2 recombinant protein was used to immunize two rabbits, yielding antisera UP2562 and UP2563 (Cocalico

Biologicals Inc.). Affinity-purified antiserum UP2563 was used for immunofluorescence and western blotting analyses in this study.

Purification of pachytene spermatocytes by STA-PUT—Pachytene spermatocytes were purified from control (*Ythdc2*$^{fl/-}$; heterozygote) and *Ythdc2*^{iKO} adult testes at 2 dpt using a mini-STA-PUT method (Bellvé, 1993; Bryant et al., 2013; La Salle et al., 2009). Each purification was performed on testes from two or three adult males. Three purifications were carried out per genotype. The purified spermatocytes were examined for purity by immunofluorescence of SYCP3 and γH2AX, and DAPI staining on surface nuclear surface spreads. The spermatocyte samples with a purity of more than 80% pachytene cells were used for RNA-seq and western blot analyses.

RNA-Seq library construction and sequencing—Total RNA of the purified pachytene spermatocytes was extracted using Trizol reagent (Ambion) according to the manufacturer's instructions. The RNA quality and quantity were assessed using the Agilent 2100 Bioanalyzer. The cDNA library was constructed with 3 μg of input total RNA for each sample using the Illumina TruSeq RNA Sample Preparation Kit according to the manufacturer's instructions. The peak and average final fragment sizes were ~280 bp and ~400 bp, respectively. Three libraries for *Ythdc2*$^{fl/-}$ pachytene cells and three libraries for *Ythdc2*^{iKO} pachytene cells were generated (Table S1). 100-cycle single-end sequencing of the libraries was performed on Illumina NovaSeq 6000 (Illumina, San Diego, USA) at the Next-Generation Sequencing Core (NGSC) at the University of Pennsylvania.

Bioinformatic analysis—Reads were mapped to the mouse genome (GRCm38, Ensembl release 95) using salmon v1.3.0 (salmon quant with options -l A –validateMappings–gcBias) (Patro et al., 2017). Further analysis was performed using R (https://www.r-project.org/) version3.6.3 and Bioconductor (https://bioconductor.org/). The DESeq function of DESeq2_1.25.10 bioconductor package (Love et al., 2014) was used to obtain log2 fold changes of gene expression between control (*Ythdc2*$^{fl/-}$) and mutant (*Ythdc2*^{iKO})samples and the adjusted *P value*s. Adjusted *P value* 0.1 was used as a threshold for statistical significance. Only protein-coding genes with average expression ≥ 50 reads (basemean using DESeq2 normalized read counts) across samples were analyzed. Basemean is the average of the normalized count values, dividing by size factors, taken over all samples (Table S2). In MA plots the genes with significantly different expression between the *Ythdc2*^{iKO} and control samples with log2 fold change ≥ 0.5 or ≤ (-0.5) were highlighted. The volcano plots were plotted using EnhancedVolcano function from EnhancedVolcano 1.3.5 package (https://github.com/kevinblighe/EnhancedVolcano). Significantly differentially expressed genes with the log2 fold change ≥ 0.5 or ≤ (-0.5) in the *Ythdc2*^{iKO} were highlighted. The group of genes found to be significantly up- or downregulated in the *Ythdc2*^{iKO} were searched for enriched Gene Ontology terms using ENRICHR (Chen et al., 2013; Kuleshov et al., 2016) and the enriched categories were shown. To find out whether the dysregulated genes in the *Ythdc2*^{iKO}, are expressed in the specific spermatogenic populations, we re-analyzed the published dataset containing gene expression data for spermatogonial stem cells, spermatocytes, and round spermatids (ENA: PRJEB15333) (Davis et al., 2017) and plotted the expression of *Ythdc2*$^{iKO-}$ dysregulated genes in these populations. To see

whether the *Ythdc2*^{iKO} dysregulation correlates with the transcript m^{6}A levels, we compared the *Ythdc2*^{iKO} expression changes between the genes reported to be enriched or depleted of m^{6}A (GSE102346) (Wojtas et al., 2017). RNA-seq data of pachytene spermatocytes were deposited to GEO under GSE166568.

qRT-PCR analysis—Testes and pachytene spermatocytes from control (*Ythdc2*$^{fl/-}$) and *Ythdc2*^{iKO} (*Ythdc2*$^{f/-}$ *Ddx4*-Cre^{ERT2}) adult mice at 2 dpt were used for total RNA extraction. 1 μg of total RNA from each sample was treated with RNase-free DNase I (Thermo Fisher Scientific Inc., USA), used for reverse transcription using the RevertAid First Strand cDNA Synthesis Kit (Thermo Fisher Scientific Inc., USA) with oligo(dT)$_{18}$ primers in a final volume of 20 μl, and diluted by addition of 80 μL H_2O. The quantitative real-time reverse transcription PCR (qRT-PCR) was performed using the PowerUp™ SYBR Green master mix (Applied Biosystems, Thermo Fisher Scientific Inc., USA) according to the manufacturer's instructions in technical triplicate for each gene in an optical 384-well plate on the Quant-Studio Real-Time PCR 6 Flex System (Applied Biosystems). Each real-time PCR reaction (in a final volume of 10 μl) contained 5 μL 2 × SYBR Green Master Mix, 0.25 μL of each primer (10 μM), 0.5 μL cDNA, and 4.0 μL H_2O.

Primers were designed using the NCBI/Primer-BLAST with these parameters: PCR amplicon length of 100 – 250 bp, melting temperature (Tm) at approximately 60°C, and primer pair specificity check against mouse mRNA Refseq database. The $2^{-\Delta\Delta Ct}$ method was used to calculate the relative expression of genes. Gene expression levels were normalized to the *Actb* level. The specific primers used for qRT-PCR are listed in Table S3.

Western blot analysis—Adult testes or spermatocytes purified by STA-PUT were homogenized in 4 volumes of protein extraction buffer (62.5 mM Tris-HCl (pH 6.8), 3% SDS, 10% glycerol, 5% 2-mercaptoethanol). Samples were boiled at 95°C for 10–15 minutes and centrifuged at 12,000 g for 10 minutes. 30 μg of protein extracts per sample was resolved by SDS-PAGE and transferred onto nitrocellulose membranes using semi-dry transferring using iBlot system or onto polyvinylidene fluoride (PVDF) membranes by wet transferring in transfer buffer (25 mM Tris, 192 mM glycine, 0.02% SDS, 10% methanol, pH8.3). The primary antibodies used for western blotting analysis are listed in Key Resources Table.

Culture of spermatocytes and inhibitor treatment—Freshly dissected testes from 2 to 3-month-old male mice were decapsulated and placed into Krebs buffer (120 mM NaCl, 4.8 mM KCl, 25.2 mM $NaHCO_3$, 1.2 mM KH_2PO_4, 1.2 mM $MgSO_4$, 1.3 mM $CaCl_2$, and 11.1 mM dextrose) containing collagenase (0.5 mg/ml). Testicular tubules were digested at 32°C for about 10 min and were transferred into Krebs buffer containing trypsin (0.25 mg/ml) and DNase (0.02 mg/ml). Cells were incubated at 32°C for another 10 min with repeated pipetting to become single-cell suspension. The cells were passed through a 100-μm nylon mesh and washed twice in Kreb's buffer before culture.

5 x 10^6 adult mouse testicular cells were cultured in 1 mL MEMα (minimal essential media with alpha modifications) containing 5% streptomycin, 7.5% penicillin, 0.29% DL-lactic

acid sodium salt, 0.59% HEPES, and 5% fetal bovine serum in one well of a six-well plate in 5% CO_2 at 32°C. After a one-hour acclimation culture period, cells were then treated with inhibitors. All the treatments were performed three times.

For the metaphase I competency assay, testicular cells were treated with 4 μM okadaic acid (from a stock of 244 μM in ethanol). Control cultures received an equivalent volume of ethanol alone. Five hours after culture with okadaic acid, cells were harvested for nuclear spread analysis.

For the microtubule depolymerization assay, testicular cells were treated with 0.1 μg/ml nocodazole (from a stock of 0.1 mg/ml in DMSO). Control cultures received an equivalent volume of DMSO. 16 hours after nocodazole treatment in culture, cells were harvested for nuclear spread analysis.

For the actin depolymerization assay, cells were treated with 2.5 μg/ml cytochalasin D (from a stock of 2 mg/ml in DMSO) or 0.5 μM latrunculin A (from a stock of 0.5 mM in DMSO). Control cultures received an equivalent amount of DMSO. 16 hours after inhibitor treatment, cells were harvested for nuclear spread analysis.

QUANTIFICATION AND STATISTICAL ANALYSIS

Statistical analyses were performed using SPSS statistics software version 26 (IBM Corp., USA).

The data were expressed as the mean ± standard deviation (s.d.). The number of replicates (n) is described in the text and figure legends (Figures 1B, 1F, 2D, 3B, 3C, 4B, 6C, S3B, S3C, and S8B). Data were statistically analyzed with Student's *t* test (Figures 4B, 6C, and S8B). Enrichment analysis was performed with ANOVA and Tukey HSD (Figure 5C). Differences with $p < 0.05$ were considered statistically significant.

Supplementary Material

Refer to Web version on PubMed Central for supplementary material.

ACKNOWLEDGMENTS

We thank David Page for MEIOC antibody and Leslie King for help with manuscript preparation. We thank Jessica Chotiner, Yongjuan Guan, and Fang Yang for critical reading of the manuscript. This work was supported by NIH/NICHD grants R01HD069592 and P50HD068157 (P.J.W.), NIH/NIGMS grant R35GM118052 (P.J.W.), China Scholarship Council fellowship (201906275011) (R.L.), the Swiss National Science Foundation via the NCCR RNA & Disease network (51NF40_182880) (R.S.P.), National Key Research & Development Program of China (2018YFC1003400) (M.L.), the Howard Hughes Medical Institute (S.K.), and a fellowship from the Human Frontier Science Program (D.J.).

REFERENCES

Abby E, Tourpin S, Ribeiro J, Daniel K, Messiaen S, Moison D, Guerquin J, Gaillard JC, Armengaud J, Langa F, et al. (2016). Implementation of meiosis prophase I programme requires a conserved retinoid-independent stabilizer of meiotic transcripts. Nat. Commun. 7, 10324. [PubMed: 26742488]

Abe H, Alavattam KG, Kato Y, Castrillon DH, Pang Q, Andreassen PR, and Namekawa SH (2018). CHEK1 coordinates DNA damage signaling and meiotic progression in the male germline of mice. Hum. Mol. Genet. 27, 1136–1149. [PubMed: 29360988]

Abe H, Alavattam KG, Hu YC, Pang Q, Andreassen PR, Hegde RS, and Namekawa SH (2020). The initiation of meiotic sex chromosome inactivation sequesters DNA damage signaling from autosomes in mouse spermatogenesis. Curr. Biol. 30, 408–420.e5. [PubMed: 31902729]

Bailey AS, Batista PJ, Gold RS, Chen YG, de Rooij DG, Chang HY, and Fuller MT (2017). The conserved RNA helicase YTHDC2 regulates the transition from proliferation to differentiation in the germline. eLife 6, e26116. [PubMed: 29087293]

Baltus AE, Menke DB, Hu YC, Goodheart ML, Carpenter AE, de Rooij DG, and Page DC (2006). In germ cells of mouse embryonic ovaries, the decision to enter meiosis precedes premeiotic DNA replication. Nat. Genet. 38, 1430–1434. [PubMed: 17115059]

Bellvé AR (1993). Purification, culture, and fractionation of spermatogenic cells. Methods Enzymol. 225, 84–113. [PubMed: 8231890]

Bokar JA, Shambaugh ME, Polayes D, Matera AG, and Rottman FM (1997). Purification and cDNA cloning of the AdoMet-binding subunit of the human mRNA (N6-adenosine)-methyltransferase. RNA 3, 1233–1247. [PubMed: 9409616]

Brownlee PM, Chambers AL, Cloney R, Bianchi A, and Downs JA (2014). BAF180 promotes cohesion and prevents genome instability and aneuploidy. Cell Rep. 6, 973–981. [PubMed: 24613357]

Bryant JM, Meyer-Ficca ML, Dang VM, Berger SL, and Meyer RG (2013). Separation of spermatogenic cell types using STA-PUT velocity sedimentation. J. Vis. Exp. 80. 10.3791/50648.

Chen EY, Tan CM, Kou Y, Duan Q, Wang Z, Meirelles GV, Clark NR, and Ma'ayan A (2013). Enrichr: interactive and collaborative HTML5 gene list enrichment analysis tool. BMC Bioinformatics 14, 128. [PubMed: 23586463]

Clancy MJ, Shambaugh ME, Timpte CS, and Bokar JA (2002). Induction of sporulation in Saccharomyces cerevisiae leads to the formation of N6-methyladenosine in mRNA: A potential mechanism for the activity of the IME4 gene. Nucleic Acids Res. 30, 4509–4518. [PubMed: 12384598]

Cobb J, Cargile B, and Handel MA (1999). Acquisition of competence to condense metaphase I chromosomes during spermatogenesis. Dev. Biol. 205, 49–64. [PubMed: 9882497]

Conrad MN, Lee CY, Chao G, Shinohara M, Kosaka H, Shinohara A, Conchello JA, and Dresser ME (2008). Rapid telomere movement in meiotic prophase is promoted by NDJ1, MPS3, and CSM4 and is modulated by recombination. Cell 133, 1175–1187. [PubMed: 18585352]

Crisp M, Liu Q, Roux K, Rattner JB, Shanahan C, Burke B, Stahl PD, and Hodzic D (2006). Coupling of the nucleus and cytoplasm: Role of the LINC complex. J. Cell Biol. 172, 41–53. [PubMed: 16380439]

Davis MP, Carrieri C, Saini HK, van Dongen S, Leonardi T, Bussotti G, Monahan JM, Auchynnikava T, Bitetti A, Rappsilber J, et al. (2017). Transposon-driven transcription is a conserved feature of vertebrate spermatogenesis and transcript evolution. EMBO Rep. 18, 1231–1247. [PubMed: 28500258]

de Rooij DG, and de Boer P (2003). Specific arrests of spermatogenesis in genetically modified and mutant mice. Cytogenet. Genome Res. 103, 267–276. [PubMed: 15051947]

Dia F, Strange T, Liang J, Hamilton J, and Berkowitz KM (2017). Preparation of meiotic chromosome spreads from mouse spermatocytes. J. Vis. Exp. 129. 10.3791/55378.

Ding X, Xu R, Yu J, Xu T, Zhuang Y, and Han M (2007). SUN1 is required for telomere attachment to nuclear envelope and gametogenesis in mice. Dev. Cell 12, 863–872. [PubMed: 17543860]

Dominissini D, Moshitch-Moshkovitz S, Schwartz S, Salmon-Divon M, Ungar L, Osenberg S, Cesarkas K, Jacob-Hirsch J, Amariglio N, Kupiec M, et al. (2012). Topology of the human and mouse m6A RNA methylomes revealed by m6A-seq. Nature 485, 201–206. [PubMed: 22575960]

Eggan K, Akutsu H, Loring J, Jackson-Grusby L, Klemm M, Rideout WM 3rd, Yanagimachi R, and Jaenisch R (2001). Hybrid vigor, fetal overgrowth, and viability of mice derived by nuclear cloning and tetraploid embryo complementation. Proc. Natl. Acad. Sci. USA 98, 6209–6214. [PubMed: 11331774]

Guan Y, Leu NA, Ma J, Chmátal L, Ruthel G, Bloom JC, Lampson MA, Schimenti JC, Luo M, and Wang PJ (2020). SKP1 drives the prophase I to metaphase I transition during male meiosis. Sci. Adv. 6, eaaz2129. [PubMed: 32232159]

Handel MA, and Schimenti JC (2010). Genetics of mammalian meiosis: regulation, dynamics and impact on fertility. Nat. Rev. Genet. 11, 124–136. [PubMed: 20051984]

Hsu PJ, Zhu Y, Ma H, Guo Y, Shi X, Liu Y, Qi M, Lu Z, Shi H, Wang J, et al. (2017). Ythdc2 is an N^6-methyladenosine binding protein that regulates mammalian spermatogenesis. Cell Res. 27, 1115–1127. [PubMed: 28809393]

Jain D, Puno MR, Meydan C, Lailler N, Mason CE, Lima CD, Anderson KV, and Keeney S (2018). *ketu* mutant mice uncover an essential meiotic function for the ancient RNA helicase YTHDC2. eLife 7, e30919. [PubMed: 29360036]

John GB, Gallardo TD, Shirley LJ, and Castrillon DH (2008). Foxo3 is a PI3K-dependent molecular switch controlling the initiation of oocyte growth. Dev. Biol. 321, 197–204. [PubMed: 18601916]

Kasowitz SD, Ma J, Anderson SJ, Leu NA, Xu Y, Gregory BD, Schultz RM, and Wang PJ (2018). Nuclear m^6A reader YTHDC1 regulates alternative polyadenylation and splicing during mouse oocyte development. PLoS Genet. 14, e1007412. [PubMed: 29799838]

Koszul R, Kim KP, Prentiss M, Kleckner N, and Kameoka S (2008). Meiotic chromosomes move by linkage to dynamic actin cables with transduction of force through the nuclear envelope. Cell 133, 1188–1201. [PubMed: 18585353]

Kretschmer J, Rao H, Hackert P, Sloan KE, Höbartner C, and Bohn-sack MT (2018). The m^6A reader protein YTHDC2 interacts with the small ribosomal subunit and the 5'-3' exoribonuclease XRN1. RNA 24, 1339–1350. [PubMed: 29970596]

Kuleshov MV, Jones MR, Rouillard AD, Fernandez NF, Duan Q, Wang Z, Koplev S, Jenkins SL, Jagodnik KM, Lachmann A, et al. (2016). Enrichr: A comprehensive gene set enrichment analysis web server 2016 update. Nucleic Acids Res. 44 (W1), W90–97. [PubMed: 27141961]

La Salle S, Sun F, and Handel MA (2009). Isolation and short-term culture of mouse spermatocytes for analysis of meiosis. In Meiosis. Methods in Molecular Biology (Methods and Protocols. Vol. 558, Keeney S, ed. (Humana Press), pp. 279–297.

Lasman L, Krupalnik V, Viukov S, Mor N, Aguilera-Castrejon A, Schneir D, Bayerl J, Mizrahi O, Peles S, Tawil S, et al. (2020). Context-dependent functional compensation between Ythdf m^6A reader proteins. Genes Dev. 34, 1373–1391. [PubMed: 32943573]

Lee CY, Horn HF, Stewart CL, Burke B, Bolcun-Filas E, Schimenti JC, Dresser ME, and Pezza RJ (2015). Mechanism and regulation of rapid telomere prophase movements in mouse meiotic chromosomes. Cell Rep. 11, 551–563. [PubMed: 25892231]

Lewandoski M, Meyers EN, and Martin GR (1997). Analysis of Fgf8 gene function in vertebrate development. Cold Spring Harb. Symp. Quant. Biol. 62, 159–168. [PubMed: 9598348]

Lin Z, Hsu PJ, Xing X, Fang J, Lu Z, Zou Q, Zhang KJ, Zhang X, Zhou Y, Zhang T, et al. (2017). Mettl3-/Mettl14-mediated mRNA N^6-methyladenosine modulates murine spermatogenesis. Cell Res. 27, 1216–1230. [PubMed: 28914256]

Liu N, and Pan T (2016). N6-methyladenosine–encoded epitranscriptomics. Nat. Struct. Mol. Biol. 23, 98–102. [PubMed: 26840897]

Liu J, Yue Y, Han D, Wang X, Fu Y, Zhang L, Jia G, Yu M, Lu Z, Deng X, et al. (2014). A METTL3-METTL14 complex mediates mammalian nuclear RNA N6-adenosine methylation. Nat. Chem. Biol. 10, 93–95. [PubMed: 24316715]

Love MI, Huber W, and Anders S (2014). Moderated estimation of fold change and dispersion for RNA-seq data with DESeq2. Genome Biol. 15, 550. [PubMed: 25516281]

Luoh SW, Bain PA, Polakiewicz RD, Goodheart ML, Gardner H, Jaenisch R, and Page DC (1997). Zfx mutation results in small animal size and reduced germ cell number in male and female mice. Development 124, 2275–2284. [PubMed: 9187153]

Meyer KD, and Jaffrey SR (2014). The dynamic epitranscriptome: N6-methyladenosine and gene expression control. Nat. Rev. Mol. Cell Biol. 15, 313–326. [PubMed: 24713629]

Pandita TK, Westphal CH, Anger M, Sawant SG, Geard CR, Pandita RK, and Scherthan H (1999). Atm inactivation results in aberrant telomere clustering during meiotic prophase. Mol. Cell. Biol. 19, 5096–5105. [PubMed: 10373558]

Patro R, Duggal G, Love MI, Irizarry RA, and Kingsford C (2017). Salmon provides fast and bias-aware quantification of transcript expression. Nat. Methods 14, 417–419. [PubMed: 28263959]

Peters AH, Plug AW, van Vugt MJ, and de Boer P (1997). A drying-down technique for the spreading of mammalian meiocytes from the male and female germline. Chromosome Res. 5, 66–68. [PubMed: 9088645]

Reddi PP, Naaby-Hansen S, Aguolnik I, Tsai JY, Silver LM, Flickinger CJ, and Herr JC (1995). Complementary deoxyribonucleic acid cloning and characterization of mSP-10: the mouse homologue of human acrosomal protein SP-10. Biol. Reprod. 53, 873–881. [PubMed: 8547483]

Roeder GS, and Bailis JM (2000). The pachytene checkpoint. Trends Genet. 16, 395–403. [PubMed: 10973068]

Royo H, Polikiewicz G, Mahadevaiah SK, Prosser H, Mitchell M, Bradley A, de Rooij DG, Burgoyne PS, and Turner JM (2010). Evidence that meiotic sex chromosome inactivation is essential for male fertility. Curr. Biol. 20, 2117–2123. [PubMed: 21093264]

Russell LD, Ettlin RA, Sinha Hikim AP, and Clegg ED (1990). Histological and Histopathological Evaluation of the Testis (Clearwater, FL: Cache River Press).

Scherthan H (2001). A bouquet makes ends meet. Nat. Rev. Mol. Cell Biol. 2, 621–627. [PubMed: 11483995]

Schneider CA, Rasband WS, and Eliceiri KW (2012). NIH Image to Im-ageJ: 25 years of image analysis. Nat. Methods 9, 671–675. [PubMed: 22930834]

Schonhoff SE, Giel-Moloney M, and Leiter AB (2004). Neurogenin 3-expressing progenitor cells in the gastrointestinal tract differentiate into both endocrine and non-endocrine cell types. Dev. Biol. 270, 443–454. [PubMed: 15183725]

Schwartz S, Agarwala SD, Mumbach MR, Jovanovic M, Mertins P, Shishkin A, Tabach Y, Mikkelsen TS, Satija R, Ruvkun G, et al. (2013). High-resolution mapping reveals a conserved, widespread, dynamic mRNA methylation program in yeast meiosis. Cell 155, 1409–1421. [PubMed: 24269006]

Shi H, Wang X, Lu Z, Zhao BS, Ma H, Hsu PJ, Liu C, and He C (2017). YTHDF3 facilitates translation and decay of N^6-methyladenosine-modified RNA. Cell Res. 27, 315–328. [PubMed: 28106072]

Shi B, Xue J, Yin H, Guo R, Luo M, Ye L, Shi Q, Huang X, Liu M, Sha J, and Wang PJ (2019). Dual functions for the ssDNA-binding protein RPA in meiotic recombination. PLoS Genet. 15, e1007952. [PubMed: 30716097]

Shibuya H, Hernández-Hernández A, Morimoto A, Negishi L, Höög C, and Watanabe Y (2015). MAJIN links telomeric DNA to the nuclear membrane by exchanging telomere cap. Cell 163, 1252–1266. [PubMed: 26548954]

Soh YQS, Mikedis MM, Kojima M, Godfrey AK, de Rooij DG, and Page DC (2017). Meioc maintains an extended meiotic prophase I in mice. PLoS Genet. 13, e1006704. [PubMed: 28380054]

Starr DA, and Han M (2002). Role of ANC-1 in tethering nuclei to the actin cytoskeleton. Science 298, 406–409. [PubMed: 12169658]

Starr DA, and Han M (2003). ANChors away: An actin based mechanism of nuclear positioning. J. Cell Sci. 116, 211–216. [PubMed: 12482907]

Sun F, and Handel MA (2008). Regulation of the meiotic prophase I to metaphase I transition in mouse spermatocytes. Chromosoma 117, 471–485. [PubMed: 18563426]

Trelles-Sticken E, Adelfalk C, Loidl J, and Scherthan H (2005). Meiotic telomere clustering requires actin for its formation and cohesin for its resolution. J. Cell Biol. 170, 213–223. [PubMed: 16027219]

Turner JM (2015). Meiotic Silencing in Mammals. Annu. Rev. Genet. 49, 395–412. [PubMed: 26631513]

Wang X, Lu Z, Gomez A, Hon GC, Yue Y, Han D, Fu Y, Parisien M, Dai Q, Jia G, et al. (2014). N6-methyladenosine-dependent regulation of messenger RNA stability. Nature 505, 117–120. [PubMed: 24284625]

Wiltshire T, Park C, Caldwell KA, and Handel MA (1995). Induced premature G2/M-phase transition in pachytene spermatocytes includes events unique to meiosis. Dev. Biol. 169, 557–567. [PubMed: 7781899]

Wojtas MN, Pandey RR, Mendel M, Homolka D, Sachidanandam R, and Pillai RS (2017). Regulation of m^6A transcripts by the 3'→5' RNA helicase YTHDC2 is essential for a successful meiotic program in the mammalian germline. Mol. Cell 68, 374–387.e12. [PubMed: 29033321]

Xu H, Beasley M, Verschoor S, Inselman A, Handel MA, and McKay MJ (2004). A new role for the mitotic RAD21/SCC1 cohesin in meiotic chromosome cohesion and segregation in the mouse. EMBO Rep. 5, 378–384. [PubMed: 15031719]

Xu C, Wang X, Liu K, Roundtree IA, Tempel W, Li Y, Lu Z, He C, and Min J (2014). Structural basis for selective binding of m6A RNA by the YTHDC1 YTH domain. Nat. Chem. Biol. 10, 927–929. [PubMed: 25242552]

Xu C, Liu K, Ahmed H, Loppnau P, Schapira M, and Min J (2015). Structural basis for the discriminative recognition of N6-methyladenosine RNA by the human YT521-B homology domain family of proteins. J. Biol. Chem. 290, 24902–24913. [PubMed: 26318451]

Yang F, De La Fuente R, Leu NA, Baumann C, McLaughlin KJ, and Wang PJ (2006). Mouse SYCP2 is required for synaptonemal complex assembly and chromosomal synapsis during male meiosis. J. Cell Biol. 173, 497–507. [PubMed: 16717126]

Yue Y, Liu J, and He C (2015). RNA N6-methyladenosine methylation in post-transcriptional gene expression regulation. Genes Dev. 29, 1343–1355. [PubMed: 26159994]

Zaccara S, and Jaffrey SR (2020). A unified model for the function of YTHDF proteins in regulating m^6A-modified mRNA. Cell 181, 1582–1595.e18. [PubMed: 32492408]

Zhang Z, Theler D, Kaminska KH, Hiller M, de la Grange P, Pudimat R, Rafalska I, Heinrich B, Bujnicki JM, Allain FH, and Stamm S (2010). The YTH domain is a novel RNA binding domain. J. Biol. Chem. 285, 14701–14710. [PubMed: 20167602]

Zickler D, and Kleckner N (1998). The leptotene-zygotene transition of meiosis. Annu. Rev. Genet. 32, 619–697. [PubMed: 9928494]

Zickler D, and Kleckner N (2015). Recombination, Pairing, and Synapsis of Homologs during Meiosis. Cold Spring Harb Perspect. Biol Published online May 18, 2015. 10.1101/cshperspect.a016626.

Highlights

- YTHDC2 is required for meiotic progression through the pachytene stage
- YTHDC2 deficiency causes a massively dysregulated transcriptome in pachytene cells
- Altered transcripts in YTHDC2-deficient cells encode microtubule network proteins
- Depletion of YTHDC2 leads to telomere clustering in pachytene cells

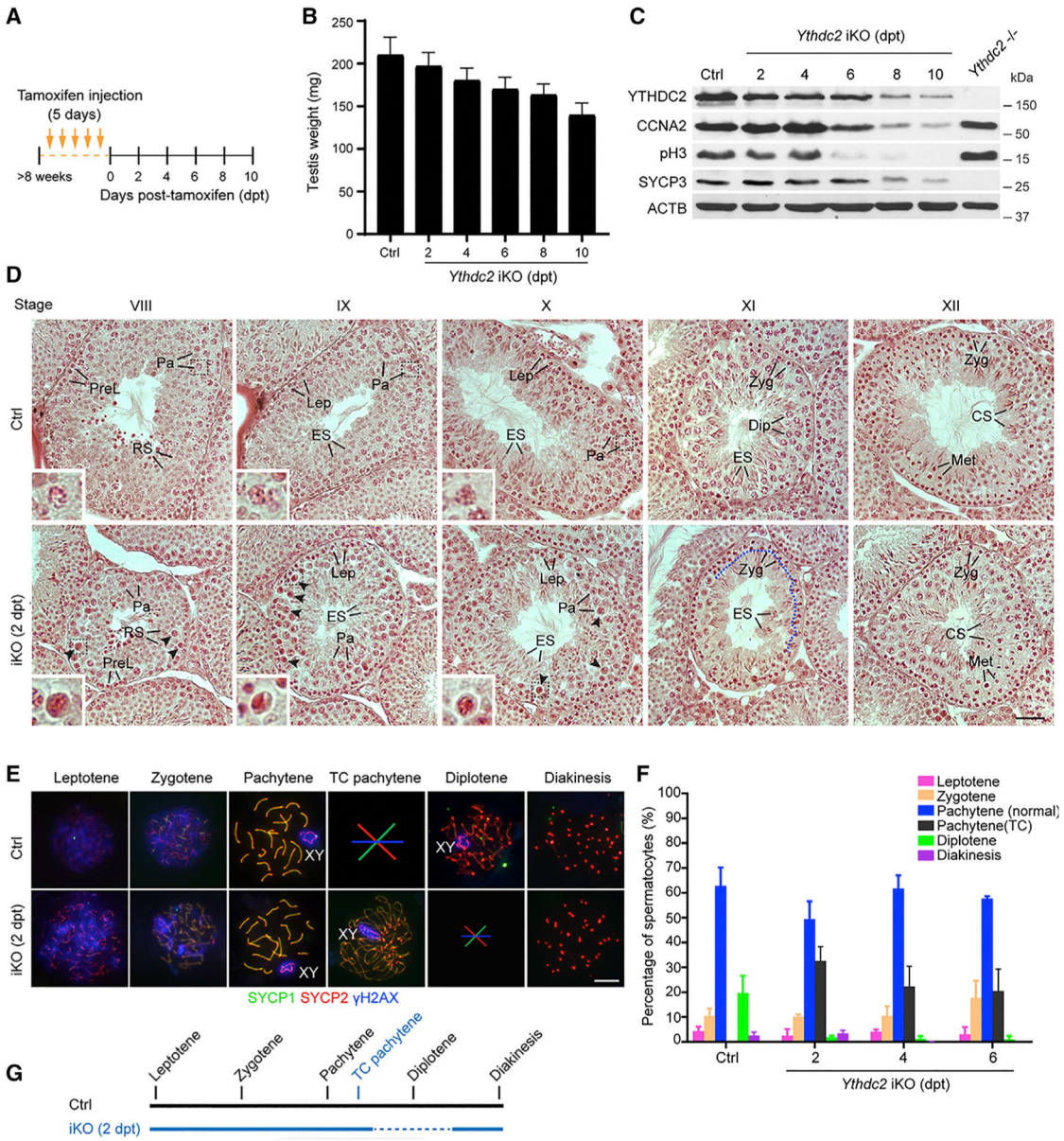

Figure 1. YTHDC2 is essential for progression through the pachytene stage

(A) Regimen of tamoxifen treatment in ≥ 8-week-old *Ythdc2*$^{fl/-}$ *Ddx4*-Cre^{ERT2} male mice. See also Figure S1.

(B) Testis weight (mean ± s.d.) of control (*Ythdc2*$^{fl/-}$, n = 16) and *Ythdc2*^{iKO} males (n = 10 at 2 dpt; 16 at 4 dpt; 3 at 6 dpt, 8 dpt, or 10 dpt).

(C) Western blot analysis of cell cycle regulators in control (*Ythdc2*$^{fl/-}$), *Ythdc2*^{iKO}, and *Ythdc2*$^{-/-}$ testes.

(D) Histology of control and *Ythdc2*^{iKO} (2 dpt) testes. Five stages of seminiferous tubules are shown (VIII-XII). Abbreviations: PreL, preleptotene; Lep, leptotene; Zyg, zygotene; Pa, pachytene; Dip, diplotene; Met, metaphase; RS, round spermatid; ES, elongating spermatid; CS, condensing spermatids. Arrowheads indicate apparently apoptotic pachytene spermatocytes, which are characterized by strong but diffuse eosin stain in the nucleus.

Insets show the boxed pachytene spermatocytes with higher magnification in stages VIII-X. Loss of diplotene spermatocytes at the stage XI *Ythdc2*^{iKO} tubule is demarcated by a dashed blue line. Scale bar, 50 μm. See also Figure S2.

(E) Surface nuclear spread analysis of control and *Ythdc2*^{iKO} (2 dpt) spermatocytes. Absence of TC pachytene cells in control is marked with a large symbol. A severe loss of diplotene cells in *Ythdc2*^{iKO} (2 dpt) is indicated by a small symbol. TC, telomere clustering.

(F) The plot shows the percentage of each type of spermatocytes in control and *Ythdc2*^{iKO} testes (mean ± s.d.) is shown. Eighty-two to 887 cells per mouse and three males per genotype per time point were analyzed. Scale bar, 10 μm.

(G) A schematic diagram of spermatocytes in control and *Ythdc2*^{iKO} (2 dpt) testes. Lines indicate the presence of spermatocytes. A thinner dash line at 2 dpt (iKO) indicates a severe reduction in the number of diplotene spermatocytes.

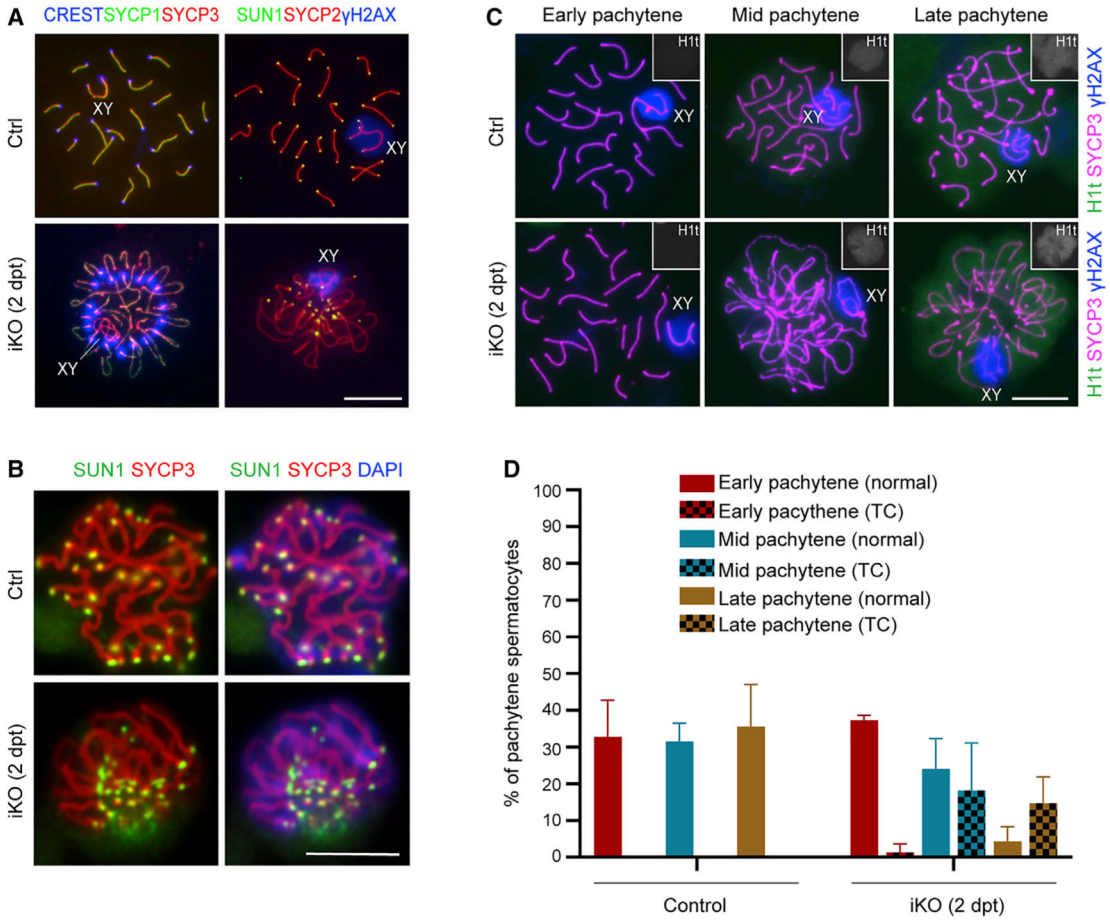

Figure 2. Telomere clustering occurs at the mid-late pachytene stage in *Ythdc2*^{iKO} spermatocytes.

(A) Immunofluorescence of CREST and SUN1 in surface nuclear spreads of pachytene cells.

(B) Immunofluorescence of SUN1 in pachytene cells prepared from testicular single cell suspension. See also Videos S1 and S2.

(C–D) Substaging of pachytene cells by the H1t expression. H1t is absent in early pachytene cells, appears in mid-pachytene cells, and is abundant in late pachytene cells (C). Inset (C) shows the H1t (black and white) signal in the entire nucleus. The plot (D) shows the percentage (mean ± s.d.) of each type of pachytene spermatocytes. Scale bars, 10 μm.

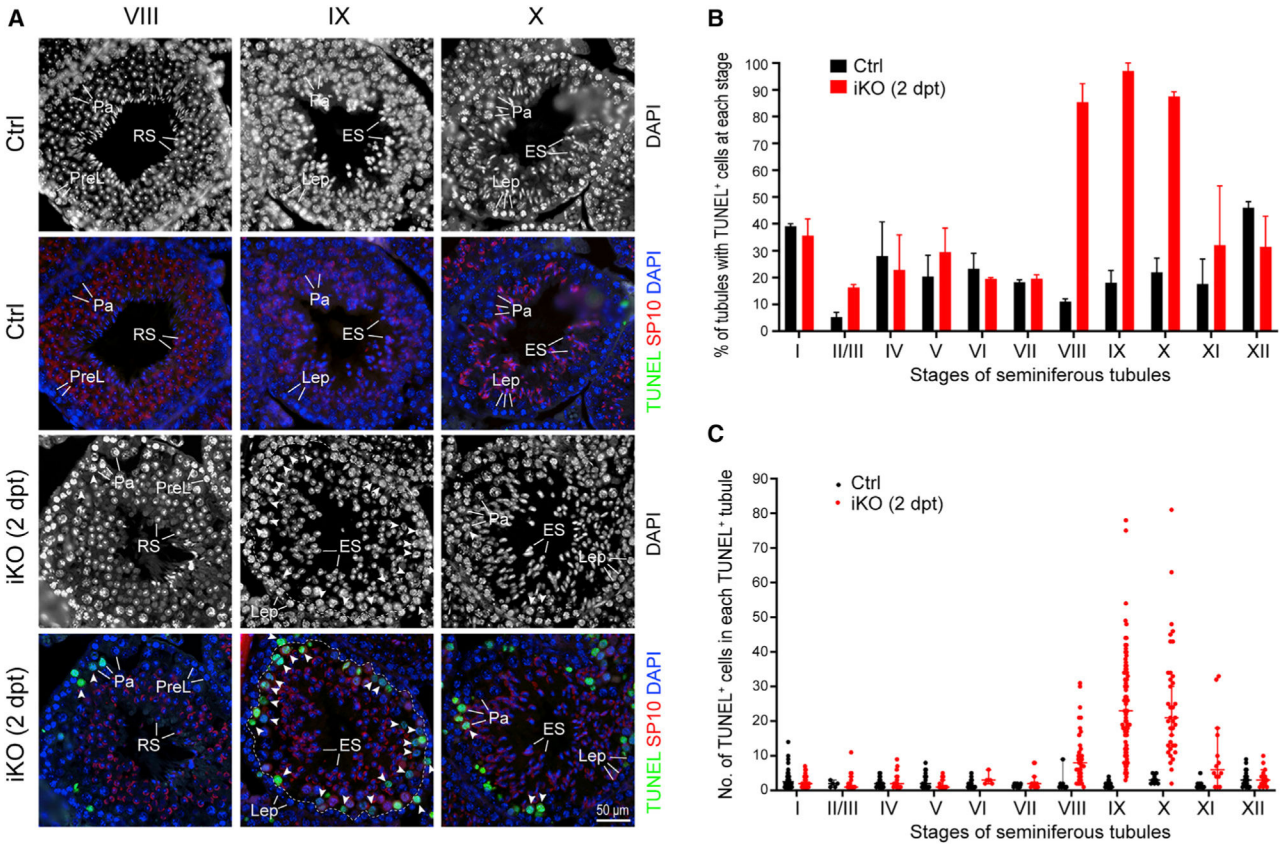

Figure 3. *Ythdc2*^{iKO} spermatocytes undergo apoptosis at the late pachytene stage

(A) TUNEL analysis of paraffin-embedded tissue sections from control and *Ythdc2*^{iKO} (2 dpt) testes. The acrosome morphology shown by SP10 immunofluorescence staining was used for seminiferous tubule staging. Nuclear DNA was stained with DAPI. Arrowheads indicate TUNEL-positive pachytene cells. The dashed line in stage IX *Ythdc2*^{iKO} demarcates pachytene cells (the inner layer) from leptotene cells (the outer layer). Abbreviations: PreL, preleptotene; Lep, leptotene; Pa, pachytene; RS, round spermatid; ES, elongating spermatid. Scale bar, 50 μm.

(B) Percentage of TUNEL-positive tubules from control and *Ythdc2*^{iKO} testes at 2 dpt. The mean ± s.d. values were plotted. Two males per genotype (control and *Ythdc2*^{iKO}) were analyzed. Three hundred twenty-three to three hundred ninety-eight tubules were counted for each mouse.

(C) Quantification of TUNEL-positive cells in TUNEL-positive tubules (mean ± s.d.) from control and *Ythdc2*^{iKO} at 2 dpt. Two males per genotype (control and *Ythdc2*^{iKO}) were analyzed. One hundred seventy-six to two hundred eighty-nine tubules were counted for each mouse.

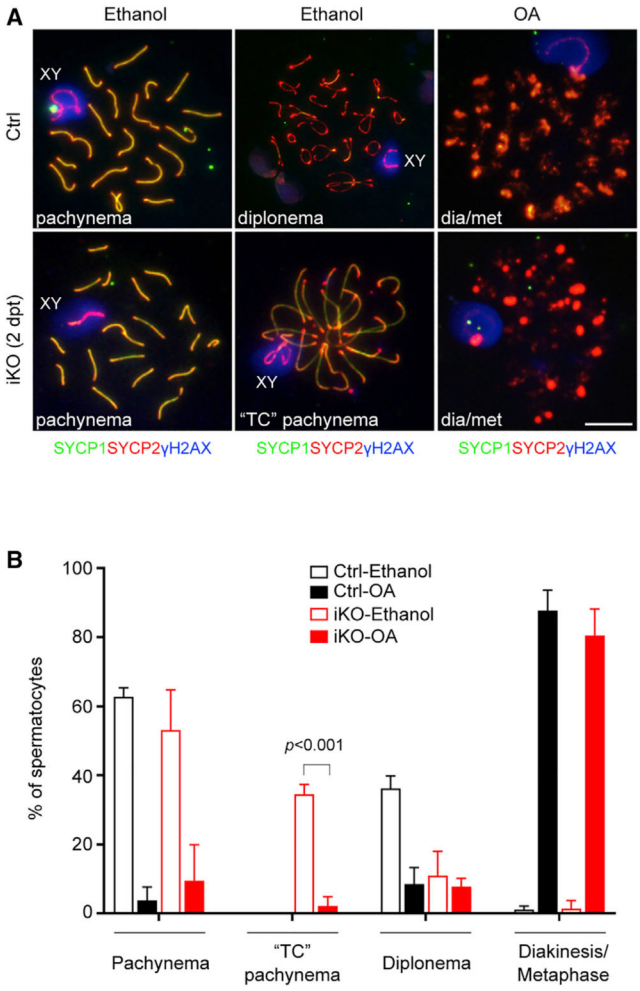

Figure 4. Meiotic progression of *Ythdc2*^{iKO} pachytene cells with telomere clustering by okadaic acid (OA) treatment

(A) Images of pachytene, diplotene, and diakinesis/metaphase I (dia/met) spermatocytes before and after OA treatment. Scale bar, 10 μm.

(B) Percentage of spermatocytes before and after OA treatment (mean ± s.d.). Only pachytene, diplotene, and diakinesis/metaphase I spermatocytes are included in this analysis. Two hundred sixty-three to eight hundred nine cells were counted per genotype per treatment group. Two males per genotype per experiment were used. The experiments were performed three times (n = 3).

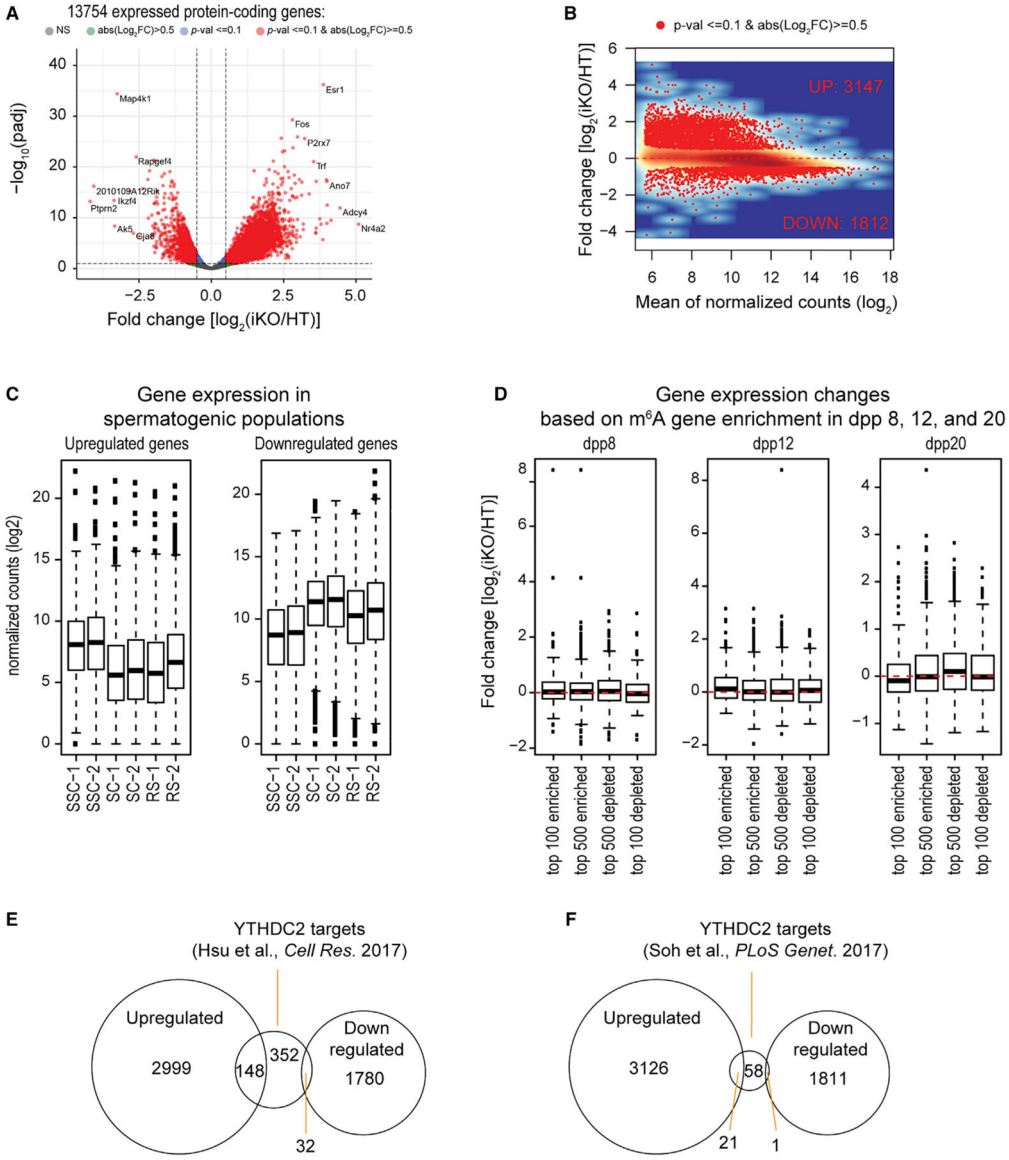

Figure 5. Dramatic alteration of transcriptome in *Ythdc2*^{iKO} pachytene spermatocytes

(A) Volcano plot of expression changes in *Ythdc2*^{iKO} versus control (*Ythdc2*$^{fl/-}$; HT) pachytene spermatocytes. Only coding genes (13,754) with an average expression of ≥ 50 normalized counts across all the samples are plotted.

(B) MA plot of expression changes. The differentially expressed (up and downregulated) genes are shown as red dots. See also Figures S4 and S5.

(C) Expression of differentially expressed genes in various wild-type spermatogenic populations. SSC, spermatogonial stem cells; SC, spermatocytes; RS, round spermatids. ANOVA was performed (*p* value < 2×10^{-16} for both upregulated and downregulated genes) and followed by TukeyHSD (*p* value < 0.001).

(D) Expression comparison of genes in *Ythdc2*^{iKO} versus control (*Ythdc2*$^{fl/-}$; HT) pachytene cells that are enriched or depleted of m^{6}A in juvenile testes (Wojtas et al., 2017).

(E) Overlap of YTHDC2 RIP-seq targets (Hsu et al., 2017) with the differentially expressed genes in *Ythdc2*^{iKO} pachytene cells.
(F) Overlap of YTHDC2 RIP-seq targets (Soh et al., 2017) with the differentially expressed genes in *Ythdc2*^{iKO} pachytene cells.

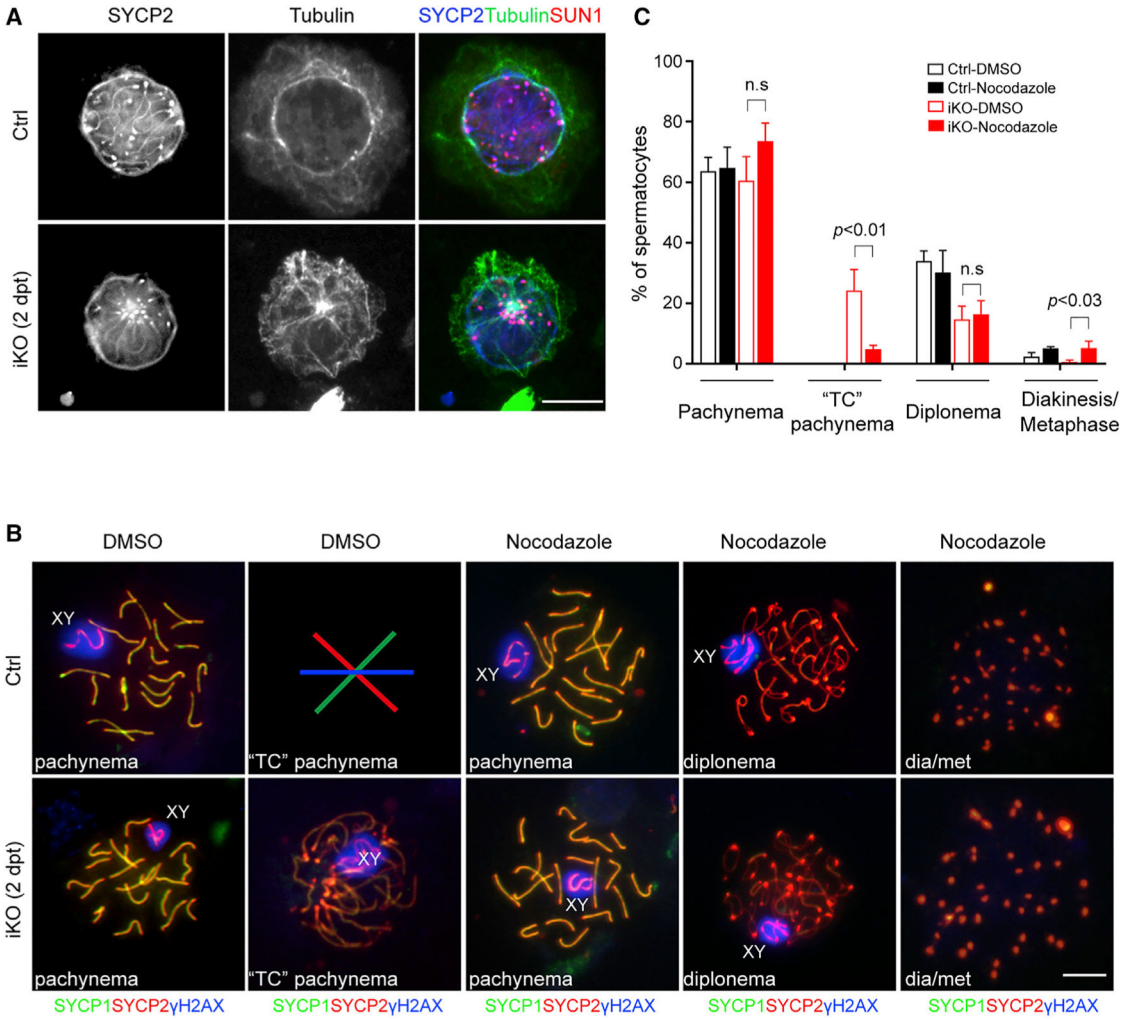

Figure 6. Inhibition of microtubule polymerization rescues telomere clustering in *Ythdc2*^{iKO} pachytene cells

(A) Immunofluorescence of α-tubulin, SUN1, SYCP2 in intact control (*Ythdc2*$^{fl/-}$) and *Ythdc2*^{iKO} (2 dpt) pachytene spermatocytes. Scale bar, 10μm. See also Figure S7.

(B) Nuclear spread analysis of pachytene, diplotene, and diakinesis/metaphase I (dia/met) spermatocytes after treatment with DMSO or nocodazole. TC, telomere clustering. Scale bar, 10μm.

(C) Percentage of spermatocytes (mean ± s.d.) in control (*Ythdc2*$^{fl/-}$) and *Ythdc2*^{iKO} (2 dpt) after treatment with DMSO or nocodazole. Only pachytene, diplotene, and diakinesis/metaphase I spermatocytes are included. Five hundred thirty-two to nine hundred eighty-five cells were counted per genotype per treatment group. Two males per genotype per experiment were used. The experiments were performed three times (n = 3). n.s., non-significant. See also Figure S8.

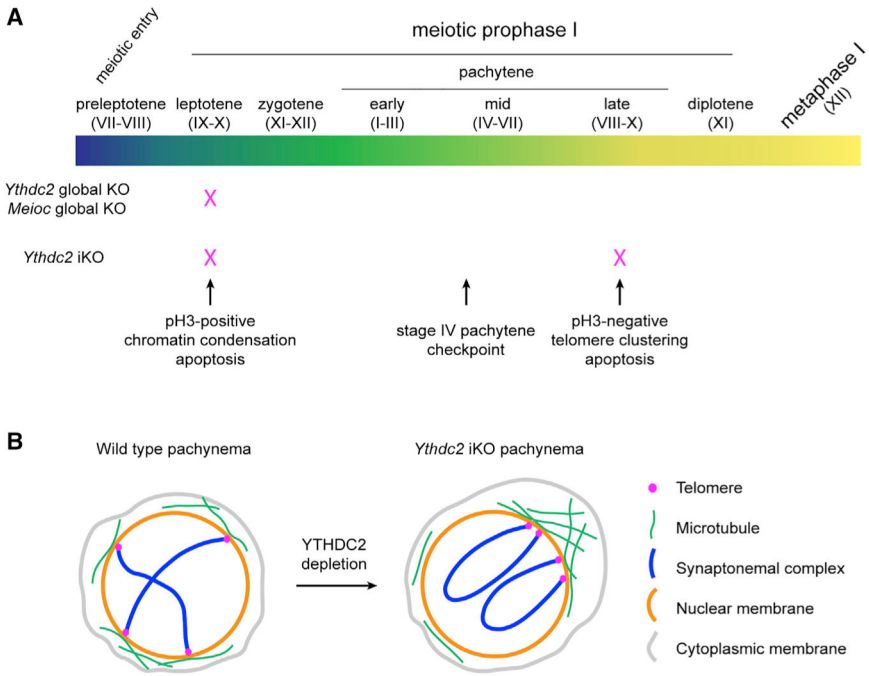

Figure 7. Stage-specific regulation of meiotic prophase I progression by YTHDC2

(A) Requirement of YTHDC2 at the leptotene and pachytene stages. The red cross designates the stage of meiotic arrest in the *Ythdc2* or *Meioc* mutants. *Ythdc2* or *Meioc* global knockout mutants display the same early meiotic arrest, which is also present in the *Ythdc2*^{iKO} (*Ythdc2*$^{fl/-}$ *Ddx4*-Cre^{ERT2}) mutant. In contrast, *Ythdc2*^{iKO} pachytene cells undergo apoptosis at the late pachytene stage. The seminiferous tubule stage is shown in Roman numerals. See also Figure S3.

(B) Illustration of telomere distribution in wild-type and *Ythdc2*^{iKO} pachytene spermatocytes. Two pairs of homologous chromosomes are depicted. The SUN/KASH proteins that connect telomeres with microtubules are not shown. In contrast with the random distribution of telomeres in wild-type, telomeres in the *Ythdc2*^{iKO} pachytene cell are clustered to one pole, where microtubules converge and the cytoplasm is expanded.

KEY RESOURCES TABLE

Reagent or resource	Source	Identifier
Antibodies		
Mouse anti-ACTB	Sigma	Cat# A5441; RRID: AB_476744
Rabbit anti-CCNA2	Abcam	Cat# ab181591; RRID: AB_2890136
Human anti-centromere (CREST)	Antibodies Incorporated	Cat# 15–234; RRID: AB_2687472
Guinea pig anti-H1t	Custom-made, a gift from Mary Ann Handel (Cobb et al., 1999)	N/A
Rabbit anti-MEIOC	Custom-made, a gift from David Page (Soh et al., 2017)	N/A
Rabbit anti-pH3	Cell Signaling Technology	Cat# 9701S; RRID: AB_331535
Guinea pig anti-SP10 (ACRV1)	Custom-made, a gift from Prabhakara Reddi (Reddi et al., 1995)	N/A
Rabbit anti-Pol II	Santa Cruz Biotechnology	Cat# sc-899; RRID: AB_632359
Rabbit anti-SUN1	Abcam	Cat# ab103021, RRID: AB_2890137
Rabbit anti-SYCP1	Abcam	Cat# ab15090; RRID: AB_301636
Guinea pig anti-SYCP2	Custom-made, (Yang et al., 2006)	N/A
Mouse anti-SYCP3	Abcam	Cat# ab97672; RRID: AB_10678841
Rabbit anti-SYCP3	ProteinTech Group	Cat# 23024–1-AP; RRID: AB_11232426
Rabbit anti-YTHDC2	Novus Biologicals	Cat# NBP1–85089; RRID: AB_11034900
Rabbit anti-YTHDC2	Custom made, this study	UP2563
Mouse anti-α-Tubulin-FITC antibody	Sigma	Cat# F2168; RRID: AB_476967
Mouse anti-γH2AX	Millipore	Cat# 16–202A; RRID: AB_568825
Chemicals, peptides, and recombinant proteins		
Tamoxifen	Sigma	Cat# T5648–1G
Okadaic acid	Cell Signaling Technology	Cat# 5934S
Nocodazole	Santa Cruz Biotechnology	Cat# sc-3518C
Colcemid	Sigma	Cat# 10295892001
Latrunculin A	Sigma	Cat# 428021–100UG
Cytochalasin D	Sigma	Cat# C8273–1MG
Deposited data		
Ythdc2 pachytene RNA-seq data	This paper	GEO: GSE166568
m^6A_seq data from mouse testes	(Wojtas et al., 2017)	GEO: GSE102346
RNA_seq profiling of mouse germ cells	(Davis et al., 2017)	ENA: PRJEB15333
Experimental models: organisms/strains		
Mouse: *Actb*-Cre	The Jackson Laboratory (Lewandoski et al., 1997)	Stock No: 003376 RRID: IMSR_JAX:003376
Mouse: *Stra8*-Cre	(Lin et al., 2017)	N/A
Mouse: *Neurog3*-Cre	The Jackson Laboratory (Schonhoff et al., 2004)	Stock No: 006333 RRID: IMSR_JAX:006333
Mouse: *Ddx4*-Cre^{ERT2}	The Jackson Laboratory (John et al., 2008)	Stock No: 024760 RRID: IMSR_JAX:024760

Reagent or resource	**Source**	**Identifier**
Mouse: *Ythdc2* fl/fl	This paper	N/A
Software and algorithms		
Adobe Creative Cloud	Adobe	https://www.adobe.com/uk/creativecloud.html
Fiji-ImageJ	(Schneider et al., 2012)	https://imagej.nih.gov/ij/
GraphPad Prism 8.0	GraphPad	https://www.graphpad.com
SPSS Statistics 26	IBM	https://www.ibm.com/products/spss-statistics